REPORT DOCUMENTATION PAGE

AFRL-SR-BL-TR-98-

0051

1. AGENCY USE ONLY (Leave blank)	2. REPORT DATE	3. REPORT TYPE AND DATES COVERED
	12/10/97	Final Technical, 8/1/93 - 7/31/97

4. TITLE AND SUBTITLE
AASERT: Graduate Student Support for Studies of Plasma Loaded Backward Wave Oscillators

5. FUNDING NUMBERS
F49620-93-10456

6. AUTHOR(S)
Y. Carmel

7. PERFORMING ORGANIZATION NAME(S) AND ADDRESS(ES)
University of Maryland, College Park
College Park, MD 20742-3511

8. PERFORMING ORGANIZATION REPORT NUMBER
N/A

9. SPONSORING / MONITORING AGENCY NAME(S) AND ADDRESS(ES)
Air Force Office of Scientific Research/PKC
110 Duncan Avenue, Suite B 115
Bolling AFB, DC 20332-8080

NE

10. SPONSORING / MONITORING AGENCY REPORT NUMBER

11. SUPPLEMENTARY NOTES

12a. DISTRIBUTION / AVAILABILITY STATEMENT
General distribution

DISTRIBUTION STATEMENT A
Approved for public release;
Distribution Unlimited

12b. DISTRIBUTION CODE

13. ABSTRACT *(Maximum 200 words)*

This grant partially supported the work of three graduate students at the Institute for Plasma Research, University of Maryland. These students actively participated in and greatly contributed to the research program on studies of plasma loaded backward wave oscillators, funded by AFOSR.

DTIC QUALITY INSPECTED 2

19980115 214

14. SUBJECT TERMS	15. NUMBER OF PAGES
Plasma Backward Wave Oscillators	55
	16. PRICE CODE

17. SECURITY CLASSIFICATION OF REPORT	18. SECURITY CLASSIFICATION OF THIS PAGE	19. SECURITY CLASSIFICATION OF ABSTRACT	20. LIMITATION OF ABSTRACT

FINAL TECHNICAL REPORT

AASERT: Graduate Student Support for Studies of Plasma Loaded Backward Wave Oscillators

AFOSR Grant Number: F49620-93-10456
"Parent" Award AFOSR Grant Number: F49620-92-J-0152

for the period
August 1, 1993 to July 31, 1997

Research conducted under the auspices of
Air Force Office of Scientific Research

Technical Director: Dr. Robert Barker
Telephone: (202) 767-5011

Executive summary

This grant partially supported the work of three graduate students at the Institute for Plasma Research, University of Maryland: James Weaver, David Gershon and Evan Pert. Those students actively participated and greatly contributed to the research program. Details of the main technical achievements can be found in the annual report. The work itself was presented at scientific conferences and published in refereed journals. The following selected publications are attached as an appendix to this document:

1) "Plasma Influence on the Dispersion properties of Finite-Length, Corrugated Waveguides", A. Shkvarunets, S. Kobayashi, J. Weaver, Y. Carmel, J. Rogers, T. Antonsen,, V. L. Granatstein, W.W. Destler, K. Ogura, and K. Minami, Physical Review E., 53, 3 (1996).

2) "Electromagnetic Properties of Corrugated and Smooth Waveguides Filled with Radially Inhomogeneous Plasma", A. Shkvarunets, S. Kobayashi, J. Weaver, Y. Carmel, J. Rogers, T. Antonsen,, V. L. Granatstein, W.W. Destler, IEEE Trans. plasma science, Special Issue on HPM, 24, 3, pp 905-918 (1996).

3) "Comparative study of microwave sintering of Zinc Oxide at 2.45, 30 and 83 GHz", A. Birnboim, D. Gershon, J. Calame, A. Birman, Y. Carmel, J. Rodgers B. Levush, Yu. V. Bykov, A.G. Eremeev, V.V. Holoptsev and V.E. Semenov, D. Dadon, L.P. Martin , M. Rosen and R. Hutcheon, accepted for publication in Journal of the American Ceramic Society (1997).

4) "Low Cost Infrared Temperature Measurement and Optimal Process Control in Microwave Sintering Systems", J.P. Calame, Y. Carmel, E. Pert and D. Gershon, 24th IEEE International Conference on Plasma science, San Diego, May 19-22, 1997, (Paper 1D01, p 159).

Appendix (copies of selected papers)

Plasma influence on the dispersion properties of finite-length, corrugated waveguides

A. Shkvarunets, S. Kobayashi, J. Weaver, Y. Carmel, J. Rodgers, T. M. Antonsen, Jr., V. L. Granatstein, W. W. Destler, K. Ogura,* and K. Minami*

Institute for Plasma Research, University of Maryland, College Park, Maryland 20742

(Received 13 October 1995)

We present an experimental study of the electromagnetic properties of transverse magnetic modes in a corrugated-wall cavity filled with a radially inhomogeneous plasma. The shifts of the resonant frequencies of a finite-length, corrugated cavity were measured as a function of the background plasma density and the dispersion diagram was reconstructed up to a peak plasma density of 10^{12} cm^{-3}. Good agreement with a calculated dispersion diagram is obtained for plasma densities below 5×10^{11} cm^{-3}.

PACS number(s): 52.40.Mj, 84.40.Fe, 52.40.Fd, 52.25.Sw

Spatially periodic electrodynamic structures are an essential part of many sources of high power, coherent, electromagnetic radiation [1]. In particular, cylindrical corrugated waveguides are used in relativistic microwave generators such as the backward wave oscillator where kinetic energy from a linear electron beam is transferred to electromagnetic waves [2–7]. The backward wave oscillator uses a finite-length corrugated cavity and a cylindrically symmetric linear relativistic electron beam. The beam interacts with the first spatial harmonic of the corrugated resonator when the phase velocity of the mode, ω/k_z, equals the longitudinal velocity of the beam, v_z.

Advantages of such oscillators are high power handling capability, frequency stability, as well as relative simplicity of beam formation, injection and propagation through the corrugated resonator. Additional capabilities include modest frequency tunability by changing the beam voltage and control of the output microwave power by changing the beam current. These two also represent limitations if greater flexibility is desired. Broadband frequency tuning is impossible and the output power is limited by deterioration in the electron beam quality as the beam current approaches a substantial fraction of the vacuum space charge limit. A promising solution to these two limitations of relativistic backward wave oscillators is to fill the beam propagation channel with a tenuous background plasma, thereby considerably changing both the beam propagation conditions and the electromagnetic properties of the system [8–14].

Beam propagation in a background plasma is affected by the ratio of the plasma electron density, N_p, to beam electron density, N_b. As this ratio increases, more of the beam self space charge field is neutralized by the background plasma, thereby reducing the space charge effects on the beam quality. Under these conditions a much larger beam current can propagate through the system without big sacrifices in beam quality (low $\Delta v_z/v_z$ ratio).

Plasma influence on the electromagnetic dispersion properties of waveguides can be described by the parameter ω_p/ω, where ω_p and ω are the electron plasma frequency and the frequency of the vacuum waveguide mode, respectively. The plasma upshifts the electromagnetic branches of vacuum TM modes in waveguides as approximately given by $\omega_0^2=\omega_p^2+\omega^2$ where ω_0 is the upshifted frequency of the plasma filled resonator. If a strong guiding magnetic field (B_z) is applied ($eB_z/\gamma m \gg \omega_0, \omega_p$), only TM modes will be upshifted. TE modes will remain unaffected because these modes have a zero longitudinal E_z component of electric field.

The above two properties of plasma loaded waveguides, namely frequency upshifts and greater current carrying capabilities, have been observed in experiments where microwave generators were driven by relativistic beams of electrons. Plasma filled backward wave oscillators have demonstrated both frequency upshift and efficiency enhancement [8,15,16]. In plasma filled relativistic TE_{13} gyrotron experiments both the beam current and output power were increased threefold over the corresponding vacuum case [17]. In other studies [18], plasma filled smooth waveguides served as the interaction region for relativistic plasma microwave oscillators, where the propagation of both fast ($\omega/k_z>c$) and slow ($\omega/k_z<c$) TM_{01} modes were studied.

There are many papers devoted to the calculation and measurement of the dispersion characteristics and resonant frequencies of empty corrugated cavities; but our paper reports experimental measurements of dispersion characteristics of plasma-filled, corrugated cavities. In this research we have modified the well known resonant cavity technique [19], in which the changes in the resonant frequencies of a cavity surrounding the plasma are related to the changes in the plasma density. The comparison of plasma influence on these resonances in both smooth and corrugated cavities is the main tool of the present research. In our studies we take into account two important factors: (a) the effects of radial nonuniformities in the plasma density and (b) finite-length effects in corrugated wall cavities, which leads to the formation of discrete axial modes. In a finite-length, plasma loaded structure the axial wave numbers are quantized affecting the spectral characteristics of the system. We were able to measure the full dispersion diagram of a plasma loaded, finite-length, corrugated waveguide up to a peak plasma density of 10^{12} cm^{-3}.

In the present study, plasma creation, propagation and filling of the cavities were accomplished in the same manner as in earlier work [15]. A brief description is given below while in depth information can be found in Ref. [22]. The experi-

*Permanent address: Niigata University, Niigata City, Japan.

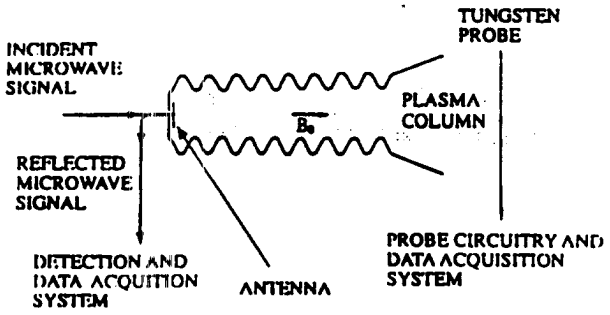

FIG. 1. A schematic diagram of a spatially periodic slow wave structure loaded with a radially inhomogeneous plasma and coupled to a radiating antenna. Also shown are the electromagnetic launcher and a long, movable tungsten probe used to measure the plasma density profile.

ments were performed in a 1.5 m long stainless-steel vacuum vessel inserted in a 1 m long solenoid producing a magnetic field of $B_z = 11.3$ kG (cyclotron frequency = 32 GHz). The plasma was generated by a coaxial flashover pulsed gun, coated with titanium hydride [20], pulsed at up to 15 kV, and positioned up to 40 cm away from one end of the solenoid. As a result, a plasma column approximately 1 m long and 2 cm in diameter was created. The plasma density profile, the electron plasma density (N_p) and temperature (T_e) are time dependent. All were measured with a long, thin movable tungsten Langmuir probe mounted perpendicular to the plasma column as shown schematically in Fig. 1. Abel's transform was used to convert the probe saturation current (taken at various radial positions) to a radial plasma density profile. The results indicate that the plasma column had roughly a bell-shaped profile with a radius, R_p, (measured at 70% peak density) of 1.2 cm at 400 μsec and 1.7 cm at 800 μsec. To illustrate temporal behavior of the plasma in the column, an oscillogram of the electron saturation probe current is presented in Fig. 2(a). The calibrated temporal dependence of the absolute peak plasma density (to be described later) is presented in Fig. 2(b), where the solid line is the plasma density averaged over many shots. A peak electron plasma density of $N_p = 1.5 \times 10^{12}$ cm^{-3} is established 200 μsec after initiation of the plasma gun, and is a monotonically decreasing function of time.

Two interchangeable plasma filled cavities—both smooth and corrugated—were studied with identical plasma loading. The corrugated cavity, shown schematically in Fig. 1, had a wall radius (R_w) varying sinusoidally according to $R_w = R_0 + h\cos(2\pi z/d)$. Here $R_0 = 1.62$ cm is the average radius, $h = 0.4$ cm is half the peak to peak amplitude of the wall corrugations, and $d = 1.66$ cm is the longitudinal period of the wall corrugation. The corrugated cavity length was $L = 14.1$ cm, which correspond to 8.5 periods. This extra half period allows coupling of the corrugated cavity to an external radiating antenna, as shown in Fig. 1. The smooth cavity used in the experiment was carefully designed to have similar resonant frequencies and mode structure as the corrugated cavity. Its radius was $R_0 = 1.62$ cm and its length $L = 15.1$ cm. The resonant frequencies in vacuum for the smooth cavity were in the range from 6.9 to 9.936 GHz and the frequency range for the corrugated cavity were from 7.4 to 8.8 GHz. The plasma column penetrated both cavities through a

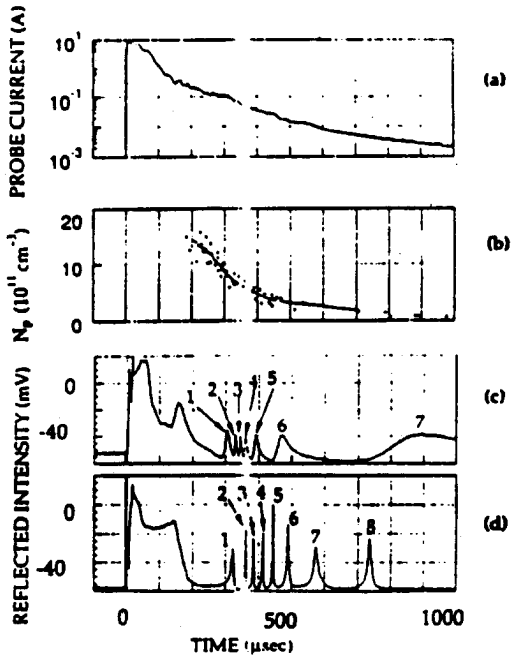

FIG. 2. The temporal evolution of (a) electron saturation current of the tungsten probe, (b) the temporal behavior of the peak plasma density—the solid line is the plasma density averaged over many shots, (c) the seven axial resonances associated with a plasma loaded, smooth-wall cavity for excitation frequency of 10 GHz, (d) the eight resonances associated with a plasma loaded, corrugated wall cavity (excitation frequency = 8.95 GHz).

diaphragm collimator with a diameter of 2 cm, which is smaller than the diameter of both the smooth and the corrugated cavities. In this way the same degree of plasma-filling was achieved in both cavities.

In this study an approach was used to study the electrodynamic properties of the cavities that took advantage of the time varying nature of pulsed plasma loading: If a fixed frequency higher than a resonant frequency of the evacuated cavity is externally applied, a dramatic change in the reflected signal occurs when the plasma density has the proper value to shift the resonance frequency up to the applied frequency. The experimental setup for measuring the reflection, shown schematically in Fig. 1, yielded the oscillograms shown in Fig. 2(c) (for smooth wall cavity) and Fig. 2(d) (for corrugated wall cavity). The large initial signal is associated with an electromagnetic wave propagating below the plasma frequency [15,18,21] and should not be confused with the cavity modes.

The research was performed in two steps. The first step was to study the shifts of the resonances of a smooth cavity due to the background plasma in order to get an independent, absolute calibration for the plasma density measured by the Langmuir probe. In the second step the shifts of the discrete resonant frequencies of the corrugated cavity were measured as a function of the background plasma density and the dispersion curve was reconstructed up to a peak plasma density of 10^{12} cm^{-3}.

The goal of the first step was to independently characterize the plasma column. A specifically developed code [22] was used to calculate the dispersion curve of TM_{01} mode in a circular, smooth infinite waveguide of radius $R_0 = 1.617$

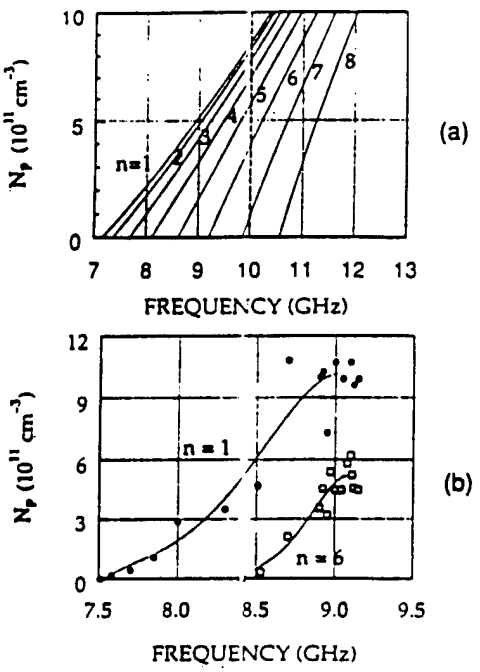

FIG. 3. (a) The calculated frequency upshifts of the eigenmodes of a smooth-wall cavity as a function of the background plasma density (the measured radial profile of the plasma density was taken into account). (b) The measured frequency upshifts of two of the eigenmodes, $n=1,6$, of a plasma loaded corrugated wall cavity.

cm, filled with radially inhomogeneous plasma of radius $R_p=1.08$ cm. The basis for the code was a numerical solution of Maxwell equations under the restrictions of azimuthal symmetry and an arbitrary plasma profile. In this work, an infinite guiding magnetic field was assumed and the plasma collimator effect (a "truncated" profile) was taken into account. The actual measured plasma profile was used, except that the plasma density was considered zero for $r>R_p$. The dispersion curve generated in this way was used to calculate the frequency shift of the TM_{01n} axial modes of a plasma filled smooth walled cavity, and the results are shown in Fig. 3(a). The solid lines correspond to resonances with axial mode number $n=1,2,\ldots,8$ from left to right. It shows that the plasma shifts the resonance frequencies of the individual axial modes. An increase in plasma density corresponds to an upward movement along the vertical axis. As an example, one can see that when the plasma density is in the range $0<N_p<9\times10^{11}$ cm^{-3}, the resonance condition can be satisfied for seven discrete TM_{01n} modes when the resonator is excited at a fixed frequency of 10 GHz (vertical dashed line). At this excitation frequency the resonance condition for mode number $n=7$ is satisfied for plasma density of $N_p=7\times10^{10}$ cm^{-3}, mode $n=6$ at $N_p=4\times10^{11}$ cm^{-3} and so on up to $n=1$ at $N_p=8.65\times10^{11}$ cm^{-3}.

In the experiment, many shots were taken to cover the frequency range from 7 up to 12 GHz (the cutoff of the TM_{02} in the corrugated cavity is about 14 GHz while in a smooth-wall cavity it is 16 GHz). Mode numbers can be assigned to the experimentally observed resonances by careful comparison of these shots and the important restriction that a mode frequency can only be upshifted by the plasma. The higher the plasma density, the higher upshift. Once the time dependent resonance for a specific injection frequency was known, the plasma density at that moment is given by the code calculation. As an example, for an applied frequency of 10 GHz, as in Fig. 2(c), the resonance condition for the TM_{017} is satisfied at $t=900$ μsec and a plasma density of $N_p=7\times10^{10}$ cm^{-3} is taken from Fig. 3(a); next is the TM_{016} at $t=473$ μsec and $N_p=4\times10^{11}$ cm^{-3} and so on up to mode TM_{011} at $t=305$ μsec and $N_p=8.65\times10^{11}$ cm^{-3}. This calibration, for many shots, shown in Fig. 2(b), was then used in the next phase of our study.

In the second step of our research the complete dispersion curve of a plasma loaded, spatially periodic, corrugated cavity was measured. The above experimental procedure was repeated, this time with a plasma-filled corrugated cavity, except that the plasma density is now known from the measurements described above. From the reflected power oscillogram shown in Fig. 2(d) (the excitation frequency is 8.95 GHz) one can see that resonant conditions for TM_{01n} modes are satisfied for $n=8$ at $t=736$ μsec, $n=7$ at $t=573$ μsec and so on up to $n=1$ at $t=323$ μsec. A series of pulsed measurements performed with different excitation frequencies were used to plot the plasma density versus the applied frequency for the discrete TM_{01n} resonances of the corrugated cavity. The final step is to assign wave numbers to the modes in order to finish constructing the dispersion diagram. The order in which the individual modes appear in the oscillogram as the applied frequency is changed clearly indicates the appropriate mode number, $n=1$ to 8. The problem of assigning resonant wave numbers, k_z, to this index was solved by using the same approach (and experimental data) presented earlier for empty cavities [23], where the resonances of evacuated closed and open (i.e., coupled to a radiating antenna) corrugated cavities were measured. Very good agreement between measurements and calculated resonant frequencies suggests that for an open corrugated cavity, the wave number k_{zn} is given by $k_{zn}=(n-1/2)\pi/L_0$ rather than $k_{zn}=n\pi/L_0$ as in the smooth close cavity case (L_0=total cavity length). Experimental data for $n=1$ and $n=6$ are presented in Fig. 3(b). Solid lines represent the result of averaging through experimental points. The lines make it possible to determine the measured dependence of resonant frequency of given resonant wave number, k_{zn}, on the plasma density. For example, if $N_p=5\times10^{11}$ cm^{-3}, the $n=1$ and $n=6$ curves in Fig. 3(b) determine that the corresponding resonance frequencies are 8.47 and 9.17 GHz, respectively.

The full result of this procedure, shown in Fig. 4, is the dispersion diagram of the plasma-filled corrugated cavity. The points connected with the solid line are experimental. The lowest curve is for $N_p=0$, the next one up is for $N_p=10^{11}$ cm^{-3} and so on for 2, 5, and 8×10^{11} cm^{-3}. The independently calculated [24] dispersion curves for an infinitely long, corrugated waveguide loaded with the same plasma densities is superimposed in the figure. The geometry used for these calculations was close to the experimental parameters ($R_p=0.75$ cm, $R_0=1.499$ cm, $h=0.406$ cm, $d=1.67$ cm). One can see that calculated frequency upshift of the dispersion curve of the TM_{01} mode due to the presence of the plasma is very close to the measured data ($\Delta\omega/\omega<2\%$) as long as the plasma density is below 5×10^{11} cm^{-3}. Above this value the measured upshift is

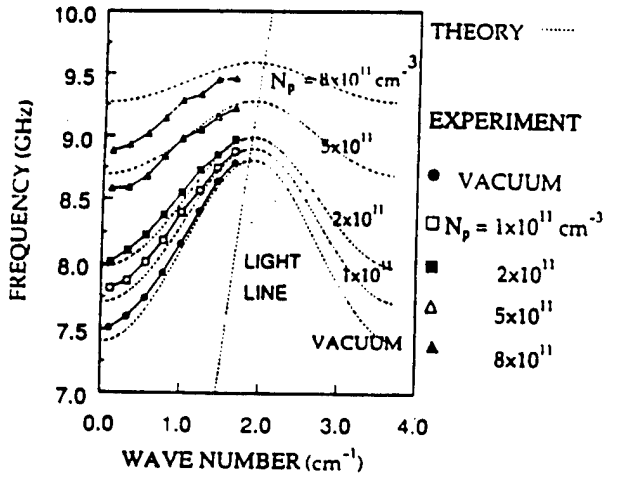

FIG. 4. The measured (points) and calculated (dashed lines) dispersion curve of a plasma loaded slow wave cavity for various background plasma densities.

somewhat less than anticipated by theory. Also, the plasma causes flattening of the dispersion diagram, especially above a plasma density of 5×10^{11} cm^{-3}, but the measured flattening is less than predicted by the calculation. The allowed passband (the difference between the upper cutoff and the lower cutoff) for the TM_{01} mode in vacuum is about 1.25 GHz. When the plasma density is 8×10^{11}, this difference is reduced to less than 0.6 GHz.

In conclusion, we were able to measure the complete dispersion curve of TM_{01n} modes of a plasma loaded, finite-length corrugated cavity. The measurement is in good agreement with calculations below peak plasma densities of 5×10^{11} cm^{-3}. Frequency shifts as high as 1.3 GHz were measured for the TM_{01} mode. It is expected that plasma effects presented in this work will enable electronic frequency tunability over a wide range (>20%) in backward wave oscillators [15] and free electron lasers [25]. Experimental and theoretical work using plasma columns in coupled cavity traveling wave tubes (CCTWT's) demonstrated the possibility of achieving a very large instantaneous bandwidth (>40%) as well as high efficiency (>35%) and high power [26].

The authors gratefully acknowledge the support of AFOSR. We thank B. Levush, G. Nusinovich, D. Goebel, and S. Miller for helpful discussions and J. Pyle and D. Cohen for technical assistance. Thanks also to ARL Adelphi personnel for their help and the use of their facilities.

[1] For example, *Applications of High-Power Microwaves*, edited by A. V. Gaponov-Grekhov and V. L. Granatstein (Artech House, Boston, 1994), Chap. 2.
[2] N. F. Kovalev *et al.*, JETP Lett. **18**, 138 (1973).
[3] Y. Carmel *et al.*, Phys. Rev. Lett. **33**, 1278 (1974).
[4] J. A. Swegle *et al.*, Phys. Fluids **28**, 2882 (1985).
[5] B. Levush *et al.*, Phys. Fluids B **4**, 2293 (1992).
[6] J. Nation, Appl. Phys. Lett. **17**, 491 (1970).
[7] S. D. Korovin *et al.* (unpublished). Also E. Schamiloglu *et al.* (unpublished).
[8] R. W. Schumacher *et al.*, in *IEEE 18th International Conference on Plasma Science* (IEEE, Piscataway, NJ, 1991), p. 135.
[9] W. R. Lou *et al.*, Phys. Rev. Lett. **67**, 18 (1991); **67**, 2481 (1991).
[10] Y. Carmel *et al.*, Phys. Rev. Lett. **62**, 2389 (1989).
[11] A. T. Lin and L. Chen, Phys. Rev. Lett. **63**, 2808 (1989).
[12] G. Benford and X. Zhai, Phys. Lett. **186**, 330 (1994).
[13] M. V. Kuzelev *et al.*, Fiz. Plazmy **13**, 1370 (1987) [Sov. J. Plasma Physics **13**, 793 (1987)].
[14] M. Button and A. Ron, Phys. Rev. Lett. **66**, 2468 (1991).
[15] Y. Carmel *et al.*, Phys. Fluids B **4**, 2286 (1992).
[16] Yu. P. Bliokh *et al.*, Fiz. Plasmy **20**, 767 (1994) [Plasma Phys. Rep **20**, 690 (1994)]; also see V. S. Ivanov *et al.*, Sov. Phys. Tech. Phys. **26**, 5 (1981).
[17] V. I. Krementsov *et al.*, JETP **75**, 2151 (1978).
[18] I. A. Selivanov *et al.*, Plasma Phys. **15**, 1283 (1989).
[19] For example, P. J. Paris *et al.*, J. Appl. Phys. **67**, 124 (1990) and references therein.
[20] A. Ben-Amar Baranga *et al.*, Rev. Sci. Instrum. **56**, 1472 (1985).
[21] A. W. Trivelpiece and R. W. Gould, J. Appl. Phys. **30**, 1784 (1959).
[22] A. G. Shkvarunets *et al.*, IEEE Trans. Plasma Science (to be published).
[23] W. Main *et al.*, IEEE Trans. Plasma Sci. **22**, 566 (1994).
[24] K. Ogura *et al.*, J. Phys. Soc. Jpn. **61**, 4022 (1992).
[25] M. R. Ried *et al.*, Int. J. Electron. **65**, 533 (1988).
[26] V. I. Perevodchikov *et al.* (unpublished).

Electromagnetic Properties of Corrugated and Smooth Waveguides Filled with Radially Inhomogeneous Plasma

Anatoly G. Shkvarunets, Satoru Kobayashi, James Weaver, Yuval Carmel, *Senior Member, IEEE*, John Rodgers, Thomas M. Antonsen, Jr., *Member, IEEE*, Victor L. Granatstein, *Fellow, IEEE*, and William W. Destler, *Fellow, IEEE*

Abstract—**Creation and diagnosis of plasma in microwave devices remains one of the primary challenges of plasma microwave electronics. In the present work we deal with 1) diagnostic techniques for characterization of radially nonuniform plasma columns suitable for use in high-power microwave sources and 2) the effects of such plasmas on the electromagnetic properties of finite length, spatially periodic slow wave structures. Experimental studies were performed both for a strong and a weak guiding magnetic field. Using a combination of a microwave resonator (X-band) and a Langmuir probe, both the plasma peak density and its transverse profile were measured *in situ* (prior to beam propagation). The frequency upshifts of the TM_{01n} modes in an open corrugated cavity were measured as a function of the background plasma density. The dispersion diagrams were reconstructed, for the first time, up to a peak plasma density of 10^{12} cm^{-3}. Frequency upshifts and "flattening" of the dispersion curves were observed for both strong and weak guiding magnetic fields. For plasma density above 5×10^{11} cm^{-3} the frequency upshifts are less than anticipated by theory.**

I. Introduction

THE FIELD of plasma microwave electronics concerns the excitation of microwaves by the injection of an electron beam into plasma [1], [2]. In many cases, plasma is introduced into an established vacuum microwave source to enhance its performance. Under these conditions, two improvements can be realized: operation at higher injected beam currents and control of the RF interaction region via the injected plasma [3]–[9]. The increase in beam current can lead to higher output powers while the latter can result in higher interaction efficiency and frequency tuning through control of plasma density in the device [8], [10], [11]. These effects have been observed in a number of devices including a plasma-filled relativistic TE_{13} gyrotron [12], a plasma-filled smooth waveguide amplifier [8], and a relativistic plasma-filled backward wave oscillator (BWO) [4], [10]. In the gyrotron experiments, both the beam current and output power were increased threefold over the vacuum case. In the plasma-filled smooth waveguide, beam injection enabled the generation of slow, $(\omega/k_z) < c$, waves [13], [14]. Here, ω, k_z, and c are the angular frequency, axial wavenumber, and speed of light, respectively.

For our studies in plasma microwave electronics we used a relativistic BWO because it is well understood, has relatively good efficiency without plasma [15]–[21], and is relatively easy to fill with plasma. Experimental work demonstrated a significant increase in operating efficiency and a tunable upshift due to the introduction of background plasma. Creation and diagnosis of plasma in microwave devices remains one of the primary challenges of plasma microwave electronics. The simplicity and high degree of ionization created by externally mounted flashover guns [26] led to their use in plasma-filled microwave BWO's [10]. Since the plasma influences the electromagnetic properties of the RF interaction region, its spatial and temporal characteristics should be known. It is the purpose of this work to develop *in situ* diagnostics to measure those properties, i.e., the axial and radial profile of the plasma density and its temporal characteristics (prior to electron beam injection). The second goal of this work is to study the electromagnetic properties of a finite length, corrugated cavity filled with radially inhomogeneous plasma. Understanding these properties will aid in developing tunable efficient plasma microwave oscillators and amplifiers.

Langmuir probes were a natural choice for measuring the spatial and temporal profiles of the plasma density, but the determination of an absolute magnitude for the density from probe data remains fundamentally incomplete due to a low accuracy of plasma density measurement. The reason is that often in magnetized plasmas particle diffusion across magnetic field is too low to prevent distortion of the plasma layer from which the probe current is being collected [23]. While the problem of distortion can sometimes be associated with an imprecise definition of the probe collection area, the flashover gun introduced further problems in that it emits ultraviolet light that created a burst of electron emission from the vessel walls and the probe itself. As a result, it was impossible to accurately measure the Volt-Ampere (V-I) probe characteristics. One more problem in measuring the absolute plasma density using a probe technique is the influence of particle energy distribution function on the probe current. The measurement of the energy distribution function of electrons is especially difficult in decaying plasmas and in the presence of ultraviolet radiation.

Manuscript received September 22, 1995; revised February 16, 1996. This work was supported by the U.S. Air Force Office for Scientific Research.

The authors are associated with the Electrical Engineering Department and the Institute for Plasma Research at the University of Maryland, College Park, MD 20742-3511 USA (email: carmel@glue.umd.edu).

Publisher Item Identifier S 0093-3813(96)05190-9.

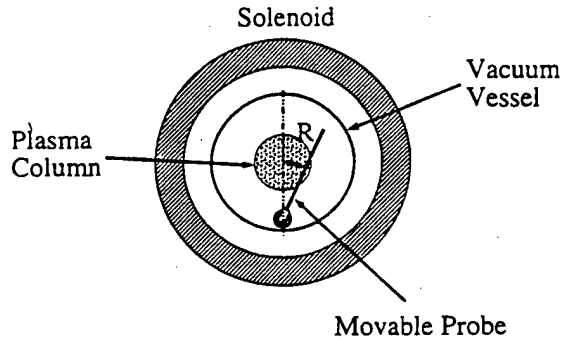

Fig. 2. Cross-sectional view of the moveable probe for measuring the transverse profile of the plasma density.

B. Diagnosis of Pulsed Plasma with a Langmuir Probe

The probe was first operated with a dc bias that was varied between shots. These experiments established two reproducible saturation levels with negative probe current (electrons) for positive biases greater than 40 V and positive probe current for negative biases less than 0 V. Attempts to plot the V-I characteristics for different moments failed because of relatively large scatter in the data. To overcome this problem, a low-impedance pulsed bias (5 μs) was applied to the probe at various times during the plasma lifetime. As a result, the electron branch of the V-I characteristic curve for different times was successfully recorded. These data are for $B = 9$ kG, for which the electron Larmour radius $\rho = 2.5 \times 10^{-3}$ mm (at $U_T = 1$ eV) is much less than the probe diameter (0.13 mm). Under these conditions the plasma may be considered highly magnetized. If the plasma electrons are thermalized, a simple one-dimensional probe theory may be used to calculate the V-I characteristic of the electron probe current

$$I(U) = I_s \exp(-U/U_T) \tag{1}$$

$$I_s = 2.7 \times 10^{-12} U_T^{1/2} \int_{S_p} n_e \, ds. \tag{2}$$

In these equations I is the probe current, U is the retarding probe potential (for electrons) relative to the plasma potential, I_s is the saturation current, U_T the electron temperature, S_p is the probe collecting area, and n_e is the electron density. Examples of the measured V-I curves for two specific moments (100 μs and 600 μs delay with respect to the plasma gun firing) are shown in Fig. 3. In the experiment, two families of V-I characteristics were observed; knee-less [Fig. 3(a)] and knee-like [Fig. 3(b)]. The first was observed for $t < 500$ μs, the second for $t > 500$ μs. The curve slope gave us the temperature in these two cases, 1.9 eV for Fig. 3(a) and 0.9 eV for Fig. 3(b). The problem was to determine the saturation current for the knee-less family of curves ($t < 500$ μs) shown in Fig. 3(a). Any current above the straight section may be considered as the saturation current, making an accurate determination of the plasma density difficult. Specifically, the plasma density from Fig. 3(a) is in the range of $1.3 - 2.7 \times 10^{12}$ cm^{-3}. In contrast, this range is much smaller in Fig. 3(b) ($1.4 - 1.5 \times 10^{11}$ cm^{-3}), for which the plasma density measured by the electromagnetic technique was 1.35×10^{11} cm^{-3}. We concluded, therefore, that a fast (5 μs)

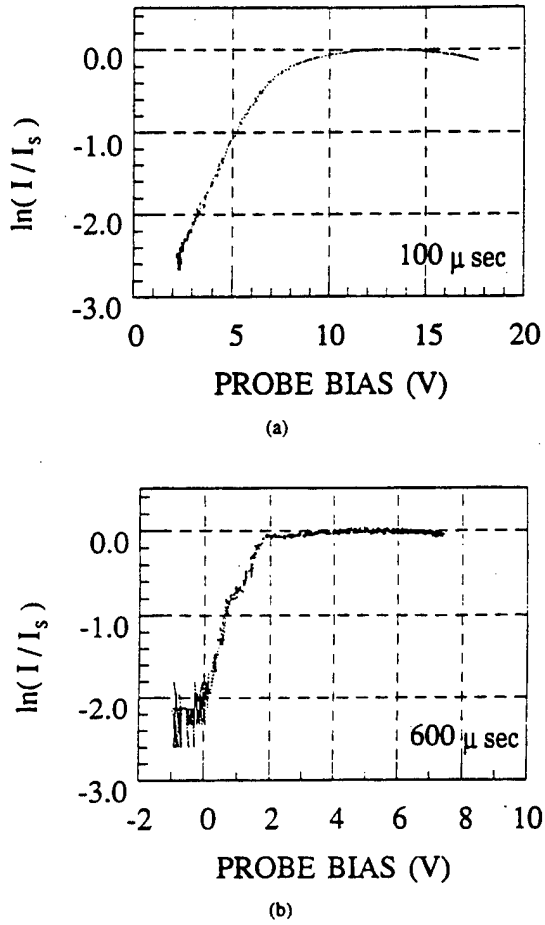

Fig. 3. Examples of typical electron branches of the V-I curves of the Langmuir probe characteristic (semilog scale). The experimental conditions: $B = 9$ kG, $U_{gun} = 11$ KV, $z_{gun} = 40$ cm. The pulsed bias ($T \sim 5$ μs) was applied at delay times of (a) 100 μs and (b) 600 μs.

pulsed Langmuir probe can be used to measure both the plasma temperature and density in the case of "classic" knee-type V-I curves. Nonideal probe characteristics are the reason for using the electromagnetic technique for independently measuring the absolute plasma density. The probe data were therefore used to measure the plasma density profile, assuming that the electron energy distribution is not dependent on radius.

The electron saturation current in the dc bias mode was used to measure the plasma density profile. The axisymmetry assumption simplifies plasma profile calculations from the probe's signal. Namely, precise specification of the chord could be abandoned and only the perpendicular distance from the probe to the central axis recorded. With this distance specified, the radial density distribution could be calculated through application of the Abel transform, thereby producing local density values from a signal that represented a set of line-integrated densities. In the experiments, the radial profile proved to have a roughly Gaussian shape. A Gaussian is invariant under the Abel inversion. Consequentially, the chord probe measurement can be treated as a plasma radial distribution function. An example of a radial profile is shown in Fig. 4. As a result of this activity we have developed the necessary tools to allow us to make relative measurements of

a reduction in the reflected signal measured by the detector and established the time at which the shifted frequencies of resonances equaled the applied frequency. Thus, the amount of shifted frequency was a controlled variable and the time for occurrence of a shifted mode was the observed variable.

Figs. 5 and 6 describe our diagnostic approach by way of a specific example. First, the relative, transverse plasma profile was measured (a typical profile is shown in Fig. 4). Next, the electron saturation current temporal dependence was measured for a fixed probe position (going through the center of the plasma column) and the result is shown in Fig. 5(a). Fig. 5(b) shows the reflected microwave signal from the smooth cavity when loaded by the same plasma column and excited by a fixed frequency ($f = 10$ GHz). These two figures give us two pieces of information: 1) the time at which each resonance condition is satisfied and 2) the probe saturation current at the same time. The last item needed to measure the absolute plasma density is given in Fig. 6, which shows the calculated resonance frequency of each of the individual axial modes (TM_{01n}, $n = 1$ to 8) as a function of the peak background plasma density. The actual measured plasma profile was used to calculate those shifted frequencies. In the calculations, the profile presented in Fig. 9(b) was used, except that plasma collimation was taken into account. The plasma density was considered to be zero for $r > R_p$ [dashed line in Fig. 9(b)]. The plasma influence and resulting time behavior is illustrated graphically in Fig. 6. In this figure the vertical line corresponds to the fixed frequency applied to the cavity (10 GHz in this example). The plasma density in the cavity decays monotonically in time, which corresponds to a downward motion along this vertical line. Since the plasma density decays monotonically in time, each subsequent resonance can then be assigned its proper mode number in sequence. The first spike in reflected signal shown in Fig. 5(b) corresponds to the intersection of the vertical line (Fig. 6) with the $n = 1$ axial mode, the second with the $n = 2$ mode, and so on until the last spike corresponds to the $n = 7$ mode. The mode number must be correctly assigned through careful choice of the excitation frequencies and comparison of separate shots.

For times less than 200 μs from plasma gun firing [Fig. 5(b)], the plasma density is large enough to enable excitation of plasma guide modes [29]. These waves can be excited if the peak plasma frequency (f_p) is higher than the externally applied frequency (f). These waves are mostly trapped inside the plasma column (see Fig. 15, case 3). Under these conditions longitudinal resonances are not expected. Therefore, for $f_p > f$, nonresonant RF losses are due to excitation of these modes as seen in Fig. 5(b). This issue was also studied in [36].

This procedure benefits us in two ways. First, we can calculate the absolute plasma density as a function of time; the result is shown in Fig. 7(a). In this case the $B_z = 9$ kG, the gun was mounted at $z_{gun} = 24$ cm and was pulsed at $U_{gun} = 14$ kV. The solid points represent the measured values, and the solid curve is an average curve through the points. The gun does have a small degree of shot-to-shot variation. The rapid plasma decay means that this variation produces the scatter seen in the plots. Second, this procedure also enables us to get

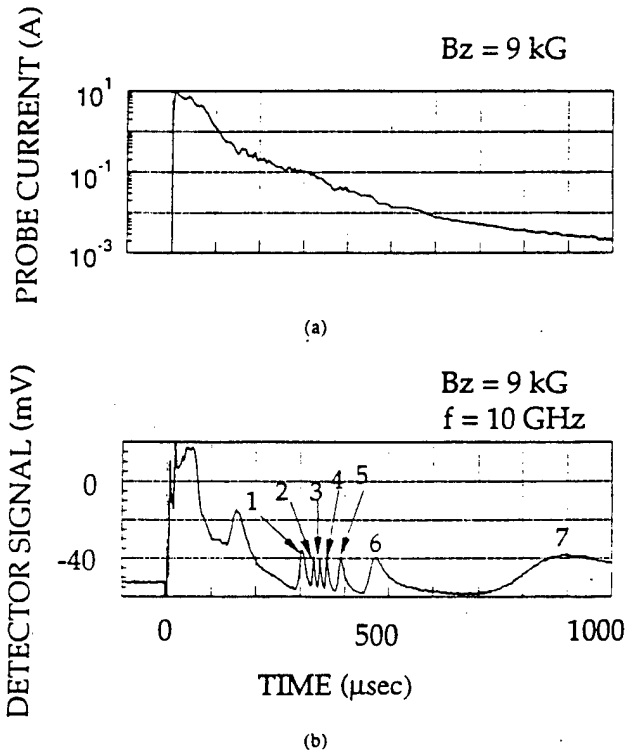

Fig. 5. (a) Temporal dependence of the electron saturation probe current for an axially positioned probe ($R = 0$). (b) Temporal dependence of the reflected microwave signal (oscillogram). The experimental conditions: $B = 9$ kG, $U_{gun} = 14$ KV, and $z_{gun} = 24$ cm.

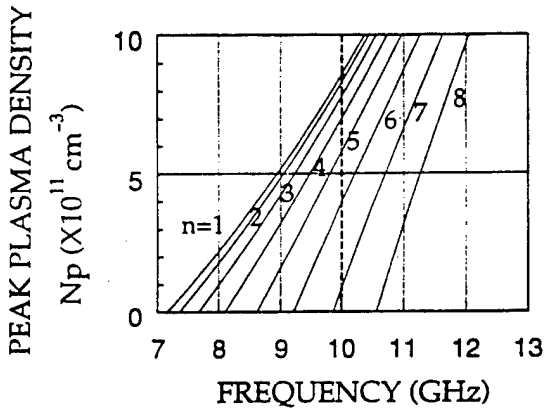

Fig. 6. The plasma influence on the longitudinal resonances of TM_{01n} modes of a plasma-filled smooth cavity, as calculated by the code (see the Appendix): $R_w = 1.6$ cm, $L = 15.1$ cm, $k_n = \pi(n/L)$, $n = 1, 2, \cdots, 8$. The transverse profile of the plasma was taken from Fig. 9(b), except that a plasma outer boundary was assumed at $r = 1.08$ cm, due to collimation by the collimator. $B_z = \infty$ was assumed.

the probe calibration curve, namely the relation between the probe current and the plasma density. Recall that previously the proportionality constant between the probe current and the plasma density was not known exactly.

III. Results from Plasma Desnity Measurements

A survey of the plasma dependence on system parameters showed that the plasma gun voltage was not seen to have a significant effect on the peak plasma density or on its radial

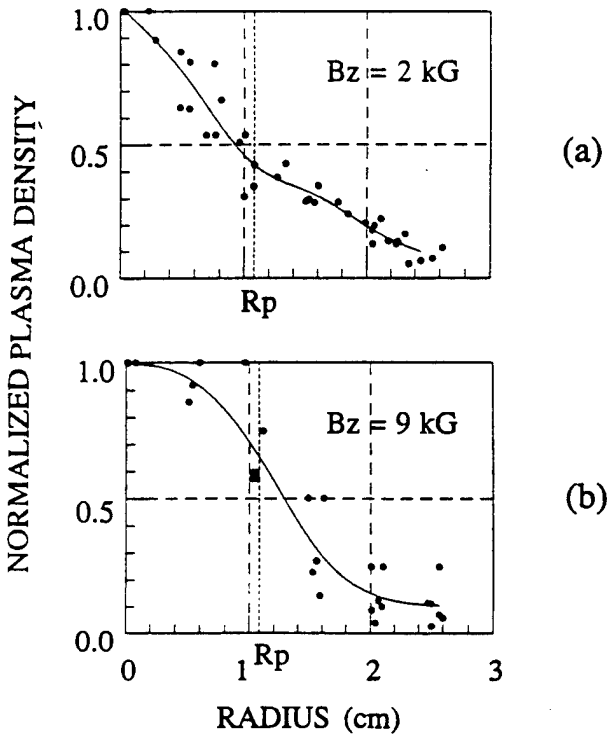

Fig. 9. The transverse profile of the plasma column outside the cavities. Experimental points are shown as black circles and the result of averaging is shown as a solid line. The vertical dashed line is the boundary of the plasma profile after the plasma collimator (profile inside the cavity). (a) $B_z = 2$ kG, $U_{gun} = 11$ kV, $z_{gun} = 40$ cm. (b) $B_z = 9$ kG, $v_{gun} = 14$ kV, $z_{gun} = 24$ cm. The profiles were used in the calculations to reconstruct the dispersion diagram of the corrugated cavity.

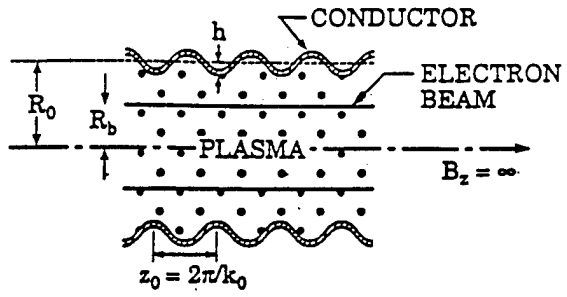

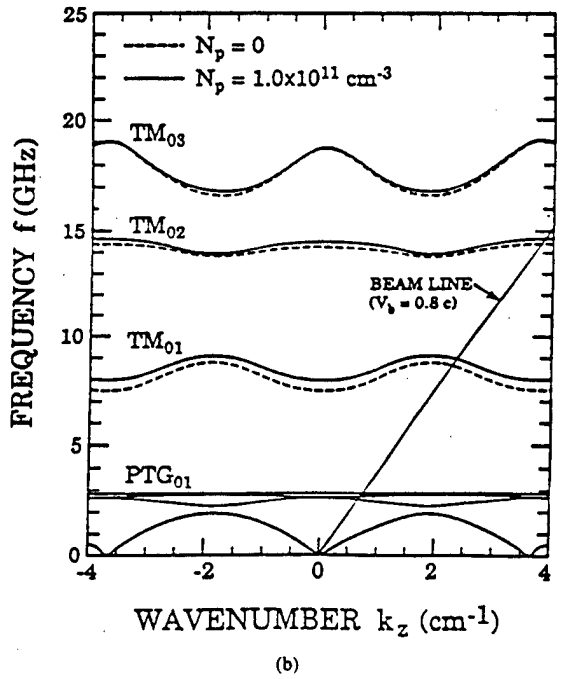

Fig. 10. (a) Schematic diagram of a corrugated-wall waveguide uniformly filled with plasma. (b) The dispersive characteristics: the upper curves are the familiar TM_{0n} family of modes modified by the plasma. The lower curves are the branches of the low frequency ($f \leq F_p = 2.84$ GHz) PTG_{01} mode [4].

filling of the waveguide, while the dashed lines correspond to the vacuum case. The passbands are upshifted as the plasma density increases. Microwave generation [14]–[21] is represented in Fig. 10(b) as the intersection of the beam line, the slope of which corresponds to the electron velocity, with the dispersion curve representing the possible modes of the structure. A new set of modes appear below the lowest passband. These modes were named periodic Trivelpiece–Gould (PTG) modes [4]. They represent an extension of the well-known Trivelpiece–Gould [29] modes of a smooth waveguide to the corrugated case. As can be seen from the diagram, the beam line also intersects the dispersion curve for these new modes. The frequency band of these modes is $0 < f < f_p$. Alternatively, these modes can be excited if $f < f_p$. In this study we emphasize examination of the plasma-induced changes in the electromagnetic properties of the TM_{01} passband ($f > f_p$), even though the PTG modes were also observed.

A sketch of the experimental configuration is shown in Fig. 11. The same antenna, circulator, oscillator, detector, and probe were used for this experiment as in the smooth cavity experiments described in Section II. The 8.5-period corrugated structure is a replica of the one used in the high power hot test experiments [10]. One end (left in Fig. 11) is a waveguide section below cutoff and the other end is a linear uptaper attached to the peak of the last half period. For these experiments a metallic end plug is used to seal the input

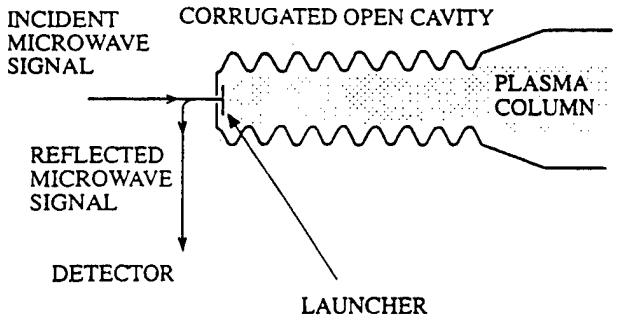

Fig. 11. Schematic diagram of a plasma-loaded open corrugated cavity experiment. The cavity is excited by a microwave signal, and the reflections are measured by a crystal detector.

waveguide and provide support for the antenna used to launch waves in the structure.

In a finite length structure, the continuous dispersion curve of TM_{01} mode of an infinitely long structure, shown in Fig. 10(b), is reduced to a number of discrete points in

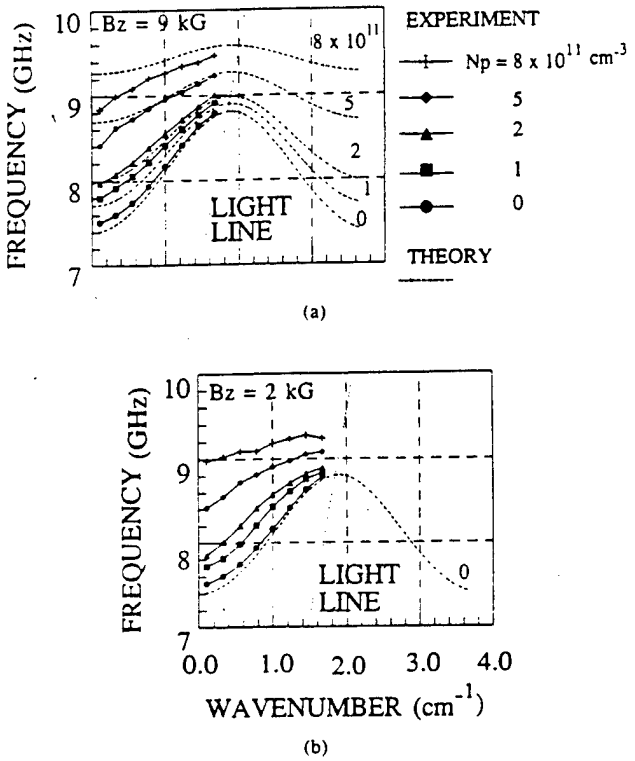

Fig. 13. Reconstructed dispersion diagrams of plasma-filled, corrugated cavity. The symbols that are connected by solid lines represent experimental data and those connected by dashed lines represent the theory [35] for a rectangular plasma column of radius 0.75 cm and $B_z = \infty$. (a) $B_z = 9$ kG, $U_{gun} = 14$ kV, $z_{gun} = 24$ cm. The peak plasma density, from the bottom up, $N_p = 0, 1, 2, 5$, and 8×10^{11} cm^{-3}. (b) $B_z = 2$ kG, $U_{gun} = 11$ kV, $z_{gun} = 40$ cm. The peak plasma density, from the bottom up, $N_p = 0, 1, 2, 5$, and 8×10^{11} cm^{-3}.

in the calculation ($R_p = .75$ cm, $R_0 = 1.499$ cm, $h = 0.406$ cm, $z_0 = 1.67$ cm). One can see that measured frequencies of the dispersion curve of the TM_{01} mode in the presence of the plasma are very close to the calculated ones ($\Delta\omega/\omega < 1\%$) for the plasma density that is below 5×10^{11} cm^{-3}. Above this value the measured upshift is less than anticipated by theory. This difference is probably due to the fact that the rectangular plasma profile used in the calculation [35] is somewhat different from the actual transverse profile, even though both have the same average radius. Also, the plasma causes flattening of the dispersion diagram, especially above a plasma density of 5×10^{11} cm^{-3}. The allowed passband (the difference between the upper cutoff and the lower cutoff) for the TM_{01} mode in vacuum is about 1.25 GHz. When the plasma density is 8×10^{11}, this difference is reduced to less than 0.5 GHz.

The result of the analysis procedure for $B_z = 2$ kG is shown in Fig. 13(b), where experimental points are connected with solid lines. The dashed line is the calculated dispersion curve for an empty corrugated waveguide. The plasma densities are $N_p = 0, 1, 2, 5$, and 8×10^{11} cm^{-3} from the bottom up. One can see that in the case of a weak magnetic field, the plasma influences the dispersion curve in much the same way as in the case of a strong magnetic field. No calculations of the $B_z = 0$ case are available for comparison. However, the results can be compared with those of a strong magnetic field.

V. Summary and Discussion

The primary challenges of plasma microwave electronics, namely the creation and diagnosis of plasmas inside high power microwave devices, can be successfully solved as demonstrated in this paper. In the present work we deal with 1) diagnostics techniques for characterization of radially nonuniform plasma columns suitable for use in high power microwave sources and 2) the effects of such plasmas on the electromagnetic properties of finite length spatially periodic slow wave structures [37] operating in X-band (8–12 GHz).

A single Langmuir probe technique cannot be used alone for precise characterization of magnetized plasma columns, especially for measurements of the electron plasma density. However, using a combination of a novel cylindrical resonant cavity technique supported by accurate numerical calculations of the plasma influence on cavity resonances and a long thin plasma probe we were able to characterize pulsed plasma columns. The peak density (higher than 10^{12} cm^{-3}) and spatial distribution (transverse and axial) of the plasma was measured as a function of the applied magnetic field (2 to 10 kG) and the plasma gun operating conditions.

By applying a combined probe-microwave technique to plasma-filled open corrugated cavities we were able to measure the complete dispersion curve of TM_{01n} modes of a plasma-loaded finite-length corrugated cavity. The measurement demonstrated the frequency upshifts and "flattening" of the dispersion curves of plasma-loaded corrugated cavities immersed in a strong guiding magnetic field, in agreement with theoretical predictions [31], [32]. It should be emphasized that these measurements describe the plasma condition and the electromagnetic properties of a plasma loaded BWO prior to electron beam injection. Other researchers [3] showed that electron beam propagation and confinement can be maintained in an unmagnetized plasma-filled BWO.

For the case of small magnetic fields, a very similar behavior was measured. Theoretical calculations for this case, however, are not readily available. Frequency shifts as high as 1.5 GHz above the vacuum frequency of 7.5 GHz (for $n = 1$) were measured. The allowed passband (the difference between the upper cutoff and the lower cutoff) for the TM_{01} mode in vacuum is about 1.25 GHz. When the plasma density is 8×10^{11} cm^{-3}, the allowed passband is reduced to less than 0.5 GHz.

Comparing the cases of high and low magnetic field demonstrated that the guiding magnetic field does not drastically affect the electromagnetic properties of both smooth-walled and corrugated plasma-loaded cavities, as long as the plasma frequency is below the signal frequency.

Both magnetized and nonmagnetized plasmas can be successfully used to fill corrugated cavities to control the electromagnetic properties and make these structures more flexible interaction regions in beam driven microwave tubes [3], [10]. Such improvements can lead to electronic frequency tunability over a wide range (>20%) in backward wave oscillators and to a significant increase in operating efficiency [10].

A plasma-loaded coupled-cavity microwave amplifier recently demonstrated [33] a large instantaneous bandwidth

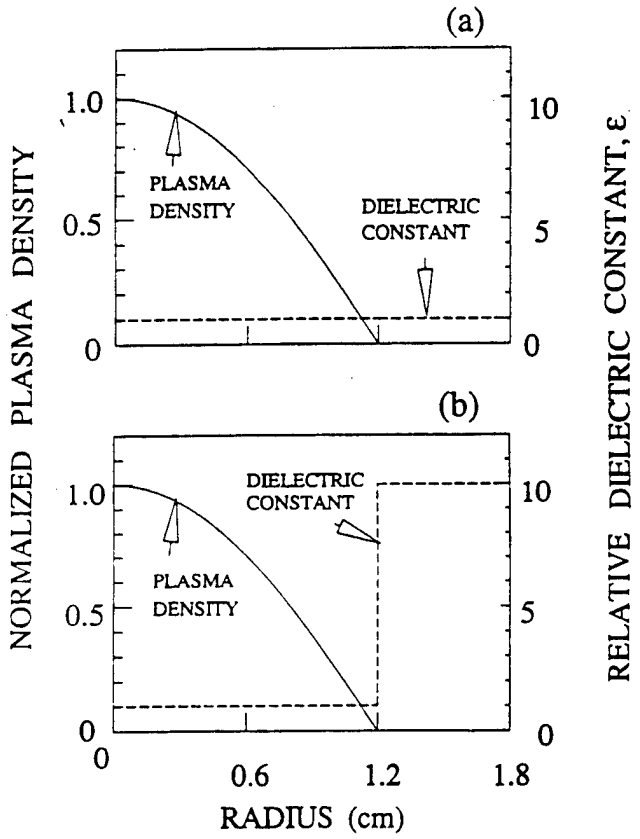

Fig. 14. The transverse profiles of the normalized plasma density (solid line) and the dielectric constant (dashed line) for: (a) a plasma-filled cylindrical waveguide; (b) a cylindrical waveguide filled with a solid dielectric and a plasma column. These profiles were used in the calculations, results of which are presented in Figs. 15 and 16.

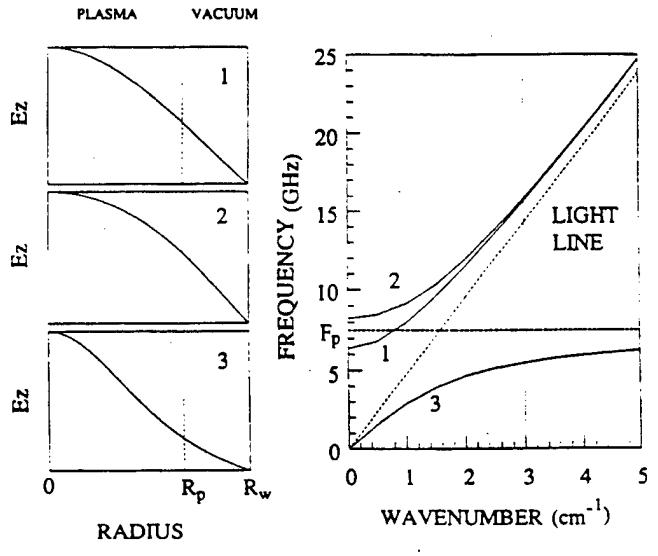

Fig. 15. Right: The dispersion curve for a cylindrical waveguide of radius $R = 1.8$ cm, loaded with a plasma column of radius $R_p = 1.2$ cm. $B_z = \infty$. Case 1: TM_{01} mode in an empty waveguide. Case 2: TM_{01} mode in a plasma-loaded waveguide. $N_p = 7 \times 10^{11}$ cm^{-3}. Case 3: Plasma guide (Trivelpiece–Gould) mode, $N_p = 7 \times 10^{11}$ cm^{-3}. Left: The transverse profiles of the longitudinal electric field, E_z. The curves labeled 1, 2, 3 are the field profiles of the corresponding cases, all calculated for $k = 3$ cm^{-1}.

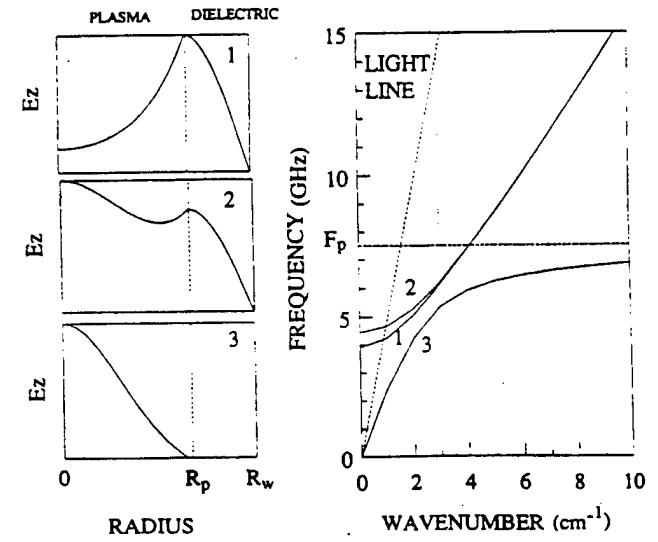

Fig. 16. Right: The dispersion curve for a cylindrical waveguide of radius $R = 1.8$ cm, loaded with a plasma column $R_p = 1.2$ cm, and a dielectric ($\epsilon = 10$)1.2 cm $< r <$ 1.8 cm. This is a model representation of a slow wave structure loaded with a plasma (see [33]). $B_z = \infty$. Case 1: TM_{01} mode in an empty waveguide. Case 2: TM_{01} mode in a waveguide loaded with plasma, $N_p = 7 \times 10^{11}$ cm^{-3}, and a dielectric ($\epsilon = 10$). Case 3: Plasma guide (Trivelpiece–Gould) mode in a waveguide loaded with plasma, $N_p = 7 \times 10^{11}$ cm^{-3}, and a dielectric ($\epsilon = 10$). Left: The transverse profile of the longitudinal electric field, E_z. The curves labeled 1, 2, 3 are the field profiles of the corresponding cases, all calculated for $k = 3$ cm^{-1}.

part of the waveguide, where the beam must propagate. As can be seen in Fig. 16 (case 1), E_z decreases significantly in the center of the waveguide because of the so-called "surface" solution for the fields. Plasma filling can improve the situation by increasing the fields in the center, as demonstrated in Fig. 16 (case 2). Moreover, by changing the plasma density, the coupling coefficient can be controlled for optimizing the system to the beam current.

The dielectric lining has very little effect on the plasma waves (compare Fig. 15, case 3 and Fig. 16, case 3). As a result, if a beam-plasma guided-waves interaction takes place in a simple plasma-filled waveguide, this interaction is expected to be only weakly dependent on the nature of the surrounding slow wave structure.

The code convergence was tested by changing the number of steps, s. The solution was found to be stable for $50 < s < 4000$. The highest sensitivity to the number of steps was found at the highest plasma density, $N_p = 2 \times 10^{12}$ cm^{-3} and a sharp plasma boundary (the case treated in the paper as a plasma-loaded smooth cavity and infinitely large magnetic field). It was found that the solution converges at $s = 3000$ and oscillates around a mean value with accuracy of $\sim 10^{-5}$. Decreasing the number of cells (s), led to a decreased accuracy. For $s = 400$, it was $\sim 10^{-4}$, and $s = 100$ gave $\sim 10^{-3}$. We chose to use $s = 400$ in our calculations, giving an accuracy of at least 10^{-4}.

ACKNOWLEDGMENT

The authors are grateful to K. Ogura and K. Minami of Niigata University for helpful discussions and performing

Satoru Kobayashi received the B.S. and M.S. degrees in geological science from Kyoto University, Japan, in 1986 and 1989, respectively, and the M.S. degree in physics from Washington State University, Pullman, in 1991. He is currently a graduate student in the Department of Physics at the University of Maryland, College Park.

James Weaver received the B.S. degree in physics from the Massachusetts Institute of Technology, Cambridge, in 1992. He is currently a graduate student in the Department of Electrical Engineering at the University of Maryland at College Park.

Yuval Carmel (S'66–M'69–SM'90), for a biography, see this issue, p. 851.

John Rodgers, for a biography, see this issue, p. 686.

Thomas M. Antonsen, Jr. (M'87), for a photograph and biography, see this issue, p. 757.

Victor L. Granatstein (S'59–M'64–SM'86–F'92), for a photograph and biography, see this issue, p. 665.

William W. Destler (M'84–SM'90–F'92), for a photograph and biography, see this issue, p. 686.

Comparative study of microwave sintering of Zinc Oxide at 2.45, 30 and 83 GHz[(a)].

A. Birnboim, D. Gershon, J. Calame, A. Birman, Y. Carmel, J. Rodgers and B. Levush,

Inst. of Plasma Research, University of Maryland, College Park, MD, USA.

Yu. V. Bykov, A.G. Eremeev, V.V. Holoptsev and V.E. Semenov

Inst. of Applied Physics, Russian Academy of Science, Nizhny Novgorod, Russia.

D. Dadon, L.P. Martin and M. Rosen

Department of Materials Science and Engineering, Johns Hopkins University, Baltimore, MD, USA.

R. Hutcheon

Chalk River Laboratories, Chalk River, Ontario K0J1J0, Canada.

(a) Parts of this work were presented at the Microwave Processing of Materials Symposium, San Francisco, CA, April 8-12, 1996, paper O3.3

Abstract

Temperature gradients that develop in ceramic materials during microwave heating are known to be strongly dependent on the applied microwave frequency. To gain better understanding of this dependence, identical samples of ZnO powder compacts were microwave heated at three distinct widely separated frequencies of 2.45, 30 and 83 GHz and the core and surface temperatures were simultaneously monitored. At 2.45 GHz, the approximately uniform "volumetric" heating tends to raise the temperature of the sample as a whole, but the interior becomes hotter than the exterior due to heat loss from the surface. At 30 and 83 GHz, this interior to exterior temperature difference was found to be reversed, especially for high heating rates. This reversal resulted from increased energy deposition close to the sample's surface associated with reduced skin depth. A model for solving Maxwell's equations was incorporated into a newly developed two-dimensional (2-D) heat transport simulation code. The numerical simulations are in agreement with the experimental results. Simultaneous application of two or more widely separated frequencies is expected to allow electronic tailoring of the temperature profile during sintering.

1. Introduction

The use of microwave energy for processing ceramics has recently become an attractive area for research and innovation. Microwave heating is volumetric, direct, instantaneous and selective. These characteristics can yield materials with improved mechanical and physical properties. Among the potential advantages of microwave processing of ceramic materials are: accelerated densification rate, controlled grain growth and uniform microstructure, achievement of high density without the use of sintering aids, improved sinterability of large bodies of complex shape, and enhanced mechanical properties. A summary of some recent studies is given in a series of review articles published in a special issue devoted to microwave processing [1].

To use these potential advantages to optimize a specific microwave sintering process, a number of technical challenges need to be addressed. For example, the approximately uniform volumetric power absorption allows a very high heating rate, but it does not guarantee a homogeneous temperature distribution. The volumetric heating uniformly raises the temperature of the entire sample, but heat loss from the surface causes the exterior to become cooler than the interior. Thus in ceramic materials with poor thermal conductivity, large thermal gradients can develop in the sample. The magnitude, sign and temporal evolution of these gradients are a function of the applied frequency. These thermal gradients, which are often negligible in conventional oven sintering, may lead to the development of undesirable density gradients during microwave sintering [2].

Fig. 1 shows the measured normalized skin-depth (the skin depth, δ, divided by the sample radius, r_{sample} = 1.6cm), as a function of temperature for ZnO at a frequency of 2.45GHz. The skin-depth is a measure of the penetration of the electromagnetic field into a material. It depends on the complex permittivity of the material ($\varepsilon = \varepsilon' - j\varepsilon''$) and on the operating frequency (f) and is given by:

$$\delta = \frac{c}{\sqrt{2}\cdot\pi\cdot f\sqrt{\sqrt{(\varepsilon')^2+(\varepsilon'')^2}-\varepsilon'}} \qquad (1)$$

where c is the velocity of light. Since δ is much larger than the sample's radius for T<700^{0}C, a quasi-homogeneous electromagnetic energy deposition inside the sample is expected. At higher temperatures and frequencies, δ decreases to less than r_{sample} (the higher the frequency the lower the value of δ). Once the skin-depth becomes much less than r_{sample} , heat deposition is concentrated at the surface, and the temperature difference ($\Delta T = T_{core}-T_{surface}$) is expected to decrease and may even become negative. Another advantage of higher frequencies is a more uniform filed distribution for a given applicator size.

At high heating rates, these gradients may cause non-uniform properties and even cracking of the sample. One possible solution to this problem , proposed in Ref. [3], is to simultaneously apply two microwave sources operating at widely separated frequencies (2.45 and 30 GHz). By dynamically and independently adjusting the output power of each of the two sources, it is possible to control the rate and spatial distribution of the energy deposition within the material being processed. This approach allows the temperature profile in the sample to be electronically "tailored" and, thereby, makes it possible to combine a high heating rate with a homogeneous temperature distribution. Also, it should be noted that the additional high frequency microwave source is expected to facilitate rapid heating of low-loss ceramics such as pure oxides and nitrides without the need for auxiliary heating, currently used in many microwave ceramic sintering applications [3].

As a first step towards the development of multi-frequency microwave heating processes, a comparative study of microwave heating of zinc oxide (ZnO) samples at 2.45, 30 and 83 GHz was performed. ZnO is widely used in the manufacture of varistors and is of commercial importance. It is particularly suitable for studies of rapid microwave sintering due to its medium loss tangent at 2.45, 30 and 83 GHz for all temperatures and its relatively low sintering temperature (1100^{0}C). In the present study, identical samples were microwave processed at the three frequencies, and for each frequency the temporal evolution of the temperature difference in the sample was measured at 15 ^{0}C/min. For 30 GHz this temperature difference was also measured at 30 and 75 ^{0}C/min. The densification curves, $\rho = \rho(T)$, were experimentally

determined for all three frequencies. Measurement of the dielectric properties, and assuming a simple temperature dependence of the thermal conductivity allowed the simulation of the microwave sintering process, with good agreement with the experimental results.

In section II the experimental set-up and procedures, as well as the results, are presented. In section III, the principles of modeling of the microwave sintering process are discussed. These include determination of the dielectric and thermal properties and their dependence on the temperature and density. In section IV, numerical simulations are presented and compared to the measurements. The final section contains a summary of the main results and conclusions of the research.

2. Microwave sintering of ZnO ceramic samples.

Identical green ZnO samples were prepared from a commercial high purity (>0.99) zinc oxide powder (particle size less than 5μm) by uniaxially binderless pressing to form cylinders 32 mm in diameter and 15 mm in height. The density of the compacted cylinders was measured to be 52% ± 2% of the crystal theoretical density (ρ_{th} = 5.61 g/cm^3). The sample was imbedded in a powdered insulation contained in an Alumina enclosure. Diagrams of the microwave sintering sample fixture and insulation, as well as a block diagram of the microwave processing furnace are shown in Figs. 2 and 3 respectively.

A sheathed, grounded type K thermocouple (outer diameter of 0.32 cm), inserted into a hole drilled into the center, measured the core temperature. The surface temperature was measured using a second type K thermocouple in contact with the cylinder's curved surface. The thermal response time of the thermocouples is under two seconds, which is short compared to the characteristic time scale of the temperature variations. Microwave sintering was performed in highly overmoded applicator equipped with a power feedback loop, shown schematically in Fig. 3. The computer regulated the rate of temperature rise (the core temperature, T_{core}, for the 2.45 GHz experiment and the surface temperature, $T_{surface}$, for 30 and 83 GHz

experiments). All samples were heated at a preset rate until a desired temperature was obtained and then cooled down. In the 2.45 GHz experiments, the microwave furnace power was reduced in a controlled way after reaching the desired maximum temperature in order to mimic the slower cool-down of a thermal oven in a previous experiments (with an initial cooling rate of ~4^{0}C/min) [2,5]. In the 30 and 83 GHz experiments, the power was turned off and the samples freely cooled down in the thermal insulation (with initial cooling rate of ~20^{0}C/min). In all cases the processing gas was air (the effect of the processing gas on the heating is discussed in Ref. [4]). All the experiments reported in this work were performed under similar conditions. Details of the processing parameters are summarized in table I. Although different powders were used as insulation in some experiments, the difference in their dielectric losses will not have a large effect on the temperatures in the sample because of their very low density.

In Fig. 4 the relative bulk density of the sintered samples, $R = \rho/\rho_{th}$, is plotted versus the maximum core temperature attained in different experiments for microwave as well as conventional heating (the issue of density gradients in the sample was addressed in [2]). The densification data for 2.45 GHz microwave heating exhibit a different behavior from that of conventional heating, as shown in Ref. [2]. Although the densification curve for 30 and 83 GHz resembles closely that of conventional oven processing, this fact does not mean that the densification rates are identical for both processes due to some differences in the cooling rate in each cases. The samples processed at 30 and 83 GHz spent somewhat less time at elevated temperatures compared to those processed in the conventional furnace.

The temperature gradients developed in the microwave heated sample depend on thermal insulation, and the intensity and spatial distribution of microwave power absorption. The spatial distribution is determined by the sample dielectric properties which are functions of the sample temperature and microwave field frequency. Thus, the temperature gradients also depend on the temperature, frequency, and heating rate. Further understanding of this dependence is critical to the successful implementation

of microwave sintering as a ceramic processing method. In the present work this dependence was studied and the results are presented below.

In Fig.5 the temperature difference ($\Delta T=T_{core}-T_{surface}$) measured at constant heating rate of 15^{0}C/min is plotted against the core temperature for three samples heated at 2.45, 30 and 83 GHz. In Fig. 6a the temperature difference ΔT is shown versus the core temperature for 30 GHz microwave heating at two heating rates, 15 ^{0}C/min and 75 ^{0}C/min. Initially, the measured temperature difference ΔT is positive and increases with the core temperature increase until a maximum value is achieved. During this initial stage the higher the heating rate the higher the value of $d\Delta T/dT_{core}$. This is confirmed by a comparison of the two traces in Fig. 6a and an analysis of the 2.45 GHz trace in Fig. 5. Fig. 5 indicates an increase in $d\Delta T/dT_{core}$ when the heating rate was abruptly changed from 1 ^{0}C/min to 15 ^{0}C/min (this occurs at T_{core} =200^{0}C). The behavior of the measured temperature difference ΔT is consistent with quasi-uniform energy deposition in the sample volume during the initial heating stage.

After peaking, the temperature difference ΔT begins to decrease while the core temperature is still rising. Such a behavior can be caused by a) a change in the power deposition profile in the sample, b) an increase in the thermal conductivity of the sample, and c) a decrease in thermal conductivity of the insulation. The first factor is related to a shorter penetration of the microwave field into the sample and is the dominant factor. At high heating rate at 30 GHz processing, a temperature reversal is observed. This reversal (negative gradient) is shown in Fig. 6b.

Ultrasonic velocity and microstructure measurements [5] were performed on selected samples in order to evaluate sample integrity and potential differences in the elastic properties. Pore shape and size have a large effect on the elastic properties, and therefore on the ultrasonic velocity of porous materials. If significantly different pore structures evolved in the samples when prepared by the different techniques, this should be manifested in differences in the velocity-density relations. The longitudinal ultrasonic velocity versus density was measured for samples heated in the conventional furnace and in microwaves at 83 and 2.45 GHz. The data of all measured samples are observed to exhibit the $v_l = v_0 (\rho/\rho_{th})^n$ behavior [5] previously found for both thermal

and 2.45 GHz microwave processed samples (n = 1.5 and v_0=6000 m/sec). The conclusion is that there is no measurable effect on the elasticity-porosity relation inherent to the use of microwave energy for sintering of this material system.

3. Modeling of Microwave Sintering of ZnO Samples

The description of the Microwave sintering process requires a combined solution of two problems related to different physical disciplines. First, one has to solve Maxwell's equations in order to get the instantaneous power deposited at each point of the system. Then the heat conductivity that is responsible for redistribution and losses of the absorbed energy has to be properly treated. Both problems are highly nonlinear as the permitivity, specific heat, conductivity coefficients and even the density and the dimensions of the sample are changing with temperature, which in itself is determined by those parameters and by the frequency and power of the microwave source. The equations describing those two processes have to be solved with complicated boundary conditions related to the detailed structure of the sample, its isolating environment and the oven.

It is obvious that such a complicated problem cannot be solved analytically, and numerical methods are required. In this section we describe the code developed in order to simulate the Microwave sintering process. The heat conduction problem is described in a two-dimensional cylindrical (r,z) geometry, thus adequate for an exact description of any configuration that has an axial symmetry. We use an orthogonal mesh with variable cell size in both r and z directions. The electromagnetic energy deposition problem is treated approximately taking into account the changes in the electromagnetic field as it penetrates into the sample. We now describe in more detail the treatment of the various physical processes involved.

3.1 Electromagnetic Energy deposition

Three dimensional [6] and ray tracing approach [7] can be used to simulate this problem. The difficulty with 3-D approach is the need for very large memory and computing time to adequately model complex and time dependent systems, especially

in highly overmoded cavities. Ray tracing is problematic because the assumption of small change in field intensity over one wavelength breaks down when modeling high loss materials (for calculation of the electromagnetic energy deposition the local, not the average, field is essential).

We calculate the energy absorption using a 1-D model, which is reasonable for heating in overmoded cavities where the electromagnetic fields are relatively uniform, leading to uniform sample illumination. The electromagnetic field penetration into the sample is calculated taking into account the instantaneous dielectric properties of the sample and its thermal insulation.

The electromagnetic power absorbed per unit volume is given by [8]

$$P=2\pi f\varepsilon_0\varepsilon''|E|^2/2 \qquad (2)$$

Where f is the applied microwave frequency, $\varepsilon = \varepsilon' - j\varepsilon''$ is the relative complex permitivity of the material, ε_0 is the permitivity of free space, and E(r,z,t) is the local complex amplitude of the microwave electric field in the material. This field is determined by the solution of the Helmholz equation

$$\nabla^2 E + \kappa^2 \cdot E = 0 \qquad (3)$$

Where $\kappa = 2\pi f\,(\mu_0\varepsilon_0\varepsilon)^{1/2}$ is the propagation vector of the electromagnetic wave and μ_0 is the free space permeability.

The dependence of the complex permitivity of ZnO on the density was discussed in great detail in [9]. In this work, however, the complex permitivity was measured during thermal heating as a function of the temperature and density. These measurements were done using a cavity perturbation technique, as reported in references [4,13]. The permitivity of ZnO, of initial density $0.52\rho_{th}$ (ρ_{th} is the theoretical density), was measured at a heating rate of 15°C/min from room temperature to ~ 1100 °C, where $\rho \cong \rho_{th}$. The results (Fig. 7) show that both the real (ε') and imaginary (ε'') parts of the complex permitivity, are fairly constant up to 700 °C and significantly increase above this temperature. In particular, ε'' changes by three orders of magnitude (from ~0.12 to ~120). In the course of heating,

densification occurs so that these measurements reflect the actual variation of the permitivity with the temperature and density for a heating rate of 15°C/min. We assumed that the material maintains its maximum permittivity value achieved during densification even during the cool down phase.

Also shown in Fig. 7 is the variation of the normalized skin-depth (δ/r_{sample}) with temperature. Note that below 700°C $\delta/r_{sample} >> 1$, which confirms the quasi-homogeneous energy deposition inside the sample at the initial stage of heating. At somewhat higher temperatures, δ/r_{sample} becomes less than unity and the higher the frequency the lower the value of δ/r_{sample}. Once $\delta/r_{sample} << 1$, heat deposition is concentrated at the sample's surface and the temperature difference ΔT drops and may become negative.

The permitivity of the Alumina casting (density of 0.24 g/cc) was taken to be

$\varepsilon = 4.5\text{-}j\cdot 0.0001$.

The room temperature permitivity of ZnO had been measured over a wide range of densities (52% - 98%) and frequencies (0.2 – 20 GHz) [5]. Both ε' and ε'', seem to exponentially decrease with respect to frequency and the slope weakly depends on the density of the sample. Since this density dependence was hard to parameterize, the same linear dependence on log(f) was assumed for all densities. The decrease in permitivity with frequency was approximated by

$$\varepsilon(f,T) = \varepsilon(2.45\text{GHz},T)\cdot[1-0.55\ \log_{10}(\ f\,(\text{GHz})\ /\ 2.45)\ ] \qquad (4)$$

This dependence was extrapolated up to 83 GHz (while keeping $\varepsilon'>1$). We note that the simulation results are not particularly sensitive to the exact frequency dependence of the permitivity, since the major factor in determining the skin-depth is the 1/f term in Eq.(1). Thus, for frequencies above 30GHz (and medium to high temperatures), the electromagnetic energy is deposited near the sample surface.

Once the complex permitivity in each cell is known we calculate the field penetration separately in the radial and axial directions using a planar approximation (the impedance matching technique). The power absorbed per unit volume in each cell

is then calculated as the sum of the contributions from both directions. Though this is only an approximate treatment it describes the main features of non-uniform absorption throughout the sample (with preferential energy absorption near the surfaces). We did not find essential differences in the conclusions of this paper about the temperature gradients, when we used only the radial energy deposition instead of both r and z contributions. This is due to the fact that at the first stages of heating the only important feature is the heat conduction, which is described exactly. At the last stages, the energy is absorbed near the surfaces of the sample, and the energy absorption through the bases of the cylindrical sample does not affect much the gradients in the radial direction.

We now describe the energy deposition due to an electromagnetic wave propagating in the z direction. For any radial position (a constant r) the 1-D wave propagation in cell i is described by two plane waves of unknown amplitudes. One is propagating in the forward direction (E_i^+) and the other in the opposite direction (E_i^-):

$$E_i = E_i^+ \exp(-j\kappa_i\xi_i) + E_i^- \exp(j\kappa_i\xi_i) \qquad (5)$$

Here $\kappa_i = 2\pi f(\mu_0\varepsilon_0\varepsilon_i)^{1/2}$ is the propagation factor of the electromagnetic wave in the i-th cell, ε_i is the relative permitivity of the i-th cell and ξ_i is the coordinate measured from the top of the i-th cell. (see Fig. 8). On the free boundary of the system the amplitude E_1^+ is assumed to be the known amplitude of the incident electromagnetic wave. The impedance method is used to solve the problem and arrive at specific values for each of the unknown wave amplitudes E_1^-, E_i^+, E_i^- [10].

The power per unit volume deposited in each cell of width d_i from this single incident wave is computed as

$$U_i = \frac{\pi f \varepsilon_0 \varepsilon''}{d_i} \int_0^{d_i} \left(\left| E_i^+ e^{-jk_i z} + E_i^- e^{jk_i z} \right|^2 \right) dz \qquad (6)$$

In order to simulate waves propagating in the opposite direction, a second incident wave of amplitude equal to the first wave (E_1^+) but uncorrected in phase is assumed to impinge on the bottom of the cylinder (see Fig 8). The total heating power deposited

in cell i is $P_i = U_i + U_{n-i+1}$. This approach allows one to find the spatial distribution of the power deposition in the system. The actual value of P_i can be calculated once the amplitude of the incident wave E_1^+ is known.

3.2 Heat conduction

The heat conduction equation in cylindrical coordinates with axial symmetry (no tangential gradients) is given by

$$\rho c_p(T)\frac{\partial T}{\partial t} = \frac{1}{r}\frac{\partial}{\partial r}(rK(T,\rho)\frac{\partial T}{\partial r}) + \frac{\partial}{\partial z}(K(T,\rho)\frac{\partial T}{\partial z} + P \qquad (7)$$

T(r,z,t) is the temperature at point (r,z) at time t, c_p and K are the specific heat and the thermal conductivity coefficient of the material occupying point (r,z) and ρ is its density. P is the absorbed power discussed in section 3.1.

A finite difference code that solves equation (7) was developed. As mentioned, we use an orthogonal mesh with variable cell size. Thus we can have small cells in the interesting regions (i.e. the sample) and wider cells in other regions. A variable mesh within a material zone enables a smooth change from small to large cells. The mesh is changing during the calculation as the sample shrinks when densification occurs.

The temperature in each cell is advanced in time by solving exactly the two-dimensional temperature field (without splitting). Several options of boundary conditions are allowed. The details of the code will be described elsewhere. In this paper we shall only describe the physical database used in the simulations presented in the next chapter.

Measurements of the thermal conductivity of ZnO after being sintered to density of 3.72 and 5.20 g/cc may be found in [11]. However, we do not have data for the conductivity during the sintering process and for the insulation. The conductivity is expected to increase during sintering, as the grains are merging and densification occurs. We modeled this behavior by a power law dependence of the conductivity on temperature. The results shown in the next chapter were obtained by describing the conductivity coefficient by

$$K = K_0 \ (T/520)^{2.5} \qquad (8)$$

where $K_0 = 5.34 \cdot 10^{-3}$ W/cm/ °C , and T is measured in °C. At low temperatures the conductivity was bounded by $K \geq 0.5\ K_0$. After densification the high conductivity obtained at 1100 °C was maintained during the cooling process. The conductivity of the insulation powder was K_0 and the conductivity of the Alumina was given by the manufacturer, and described by the function

$$K = 8 \cdot 10^{-4} + \alpha\ (T-500) \quad \text{W/cm/ °C} \qquad (9)$$

where $\alpha = 8 \cdot 10^{-7}$ for $T \leq 500$ °C and $\alpha = 16 \cdot 10^{-7}$ for $T > 500$ °C.

3.3 Specific Heat

The temperature dependence of the specific heat in the range relevant to ZnO sintering was taken from [12] and fitted to the curve [3]

$$C_p = -9880/\ T^2 + 7.43 \cdot 10^{-4}\ T + 0.58 \quad \text{J/ g/ °K} \qquad (10)$$

where T is in °K.

The specific heat of the Alumina cast was taken to be 1.09 J/ g/ °K .

3.4 Densification curve

The density of the ZnO sample is increasing during the sintering. The relative density (ρ / ρ_{th}) is not changing up to 600 °C . Above that it is given in our model by

$$(\rho / \rho_{th}) = 1 - \exp(-0.00586(T-463.7)) \quad \text{for } T \leq 1150,$$

and

$$(\rho / \rho_{th}) = 0.776 + 0.1792 \cdot 10^{-3}\ T \quad \text{for } T > 1150$$

where T is measured in °C.

The code verifies that this function in each cell is monotonically increasing and does not exceed unity.

4. Simulation of the sintering experiments

The details of the experimental setup were given in section 2. Because of symmetry it is enough to simulate a quarter of the geometry shown in Fig 2. The electromagnetic solution, however, is taking into account the full height of the system as described in 3.1.

The details of the materials and mesh used in the simulation are given in table II. The graphs presented later are the results of simulations with a total number of 5520 cells that describe the sample (initial relative density 0.52), the ZnO powder (relative density 0.12) and the Alumina cast. The mesh of the low-density powder was arranged in the z direction as a geometrical series, allowing very fine cells near the sample and broader cells far from it. Since the results converge with respect to the number of cells, it is enough to use only half the number of cells in each direction (total of ¼ number of cells). We used a mirror boundary conditions on the axes, and imposed room temperature boundary conditions on the outer surface of the Alumina cast. This is justified since our measurements show that this temperature never exceeds 100 °C.

Fig. 9 shows the measured results of a 2.45 GHz sintering (experiment z34). The three lines describe the core temperature (T_{core}), the outer boundary temperature of the sample on the equator (we shall refer to this as surface temperature ($T_{surface}$)) and the input microwave power (in W). The temperature controller was programmed to track a four segment (1, 15, -6.8 and –3.5 °C/min) T_{core} history shown in Fig.9. We see that in order to maintain the 15 °C/min heating rate, a complicated microwave power history is required. This is due to the strong temperature dependence of the ZnO permittivity on temperature. We see that when $T_{core} \approx 500$ °C, the core is further heated without power increase and even when the power is lowered. As done in the experiment a PID feedback algorithm for the input power was used in the simulation in order reproduce the desired T_{core}. Also, this new approach is advantageous because of the uncertainties in values of some physical parameters (permittivity, thermal conductivity, densification scheme) and the sensitivity of the sintering process to these parameters.

The results of our simulation are compared in details to the experiment in Figs. 10a-10d. Fig. 10a shows T_{core} from the experiment and the simulation. The two curves are almost identical. Fig. 10b compares the surface temperature. The agreement is quite good if we remember the three orders of magnitude changes in the permitivity, the non-linearity of the problem and the approximations made for the conductivity coefficients and the absorption model. A comparison of the temperature difference as a function of core temperature is given in Fig 10c. The temperature difference is rising to the same maximal value, and then decreases, though more rapidly in the simulation. Fig. 10d compares the measured input microwave power with the one used in the simulation. The plotted simulation curve is magnified by 1.33. This factor might represent energy losses in the experiment and compensate for the approximations in the calculation.

It order to investigate the behavior of the temperature difference at higher frequencies we performed similar simulations at 30 and 83 GHz. The feedback algorithm was designed to give the same T_{core} as in the 2.45 GHz calculation. The temperature difference as function of T_{core}, as calculated for 2.45, 30 and 83 GHz, is shown in Fig. 11. The temperature difference curves of all three frequencies are very similar up to 700 °C, since the conductivity dominates the process. As the permitivity starts its rapid increase, the temperature difference at 2.45 GHz rises up to 310 °C. The high frequency radiation is already completely absorbed near the surface and the temperature difference changes sign rapidly after reaching a maximal value of 190 and 170 °C, for the 30 and 83 GHz frequencies, respectively. The fact that we get a negative differences already at T_{core} of 760 °C suggests that by adding a high frequency source at this instant to the already existing 2.45GHz source will enable us to greatly reduce the temperature difference. By simultaneously using two (or more) microwave sources with an independent, dynamic power control we hope to be able to "tailor" the temperature difference during processing. To confirm this suggestion a detailed design of the power profile of both sources is needed and it should be followed by an experimental demonstration.

5. Summary and conclusion

One of the advantages of microwave processing is its ability to generate high heating rates. Unfortunately, these high heating rates tend to increase the core-surface temperature difference which are intrinsic to microwave processing. The magnitude and sign of these differences depend on the thermal and dielectric coefficients, the frequency of the applied electric field and the heating rate. Multi-frequency processing with an independent dynamic control of the power at each frequency is expected to enable external control of these gradients. In this work a comparative study of processing at three different, widely separated frequencies (2.45, 30 and 83 GHz) was reported. The temperature differences ($\Delta T = T_{core} - T_{surface}$) during heating was measured for all three frequencies. The difference increases with temperature and peaks at about T_{core} =800^{0}C. For the 30 and 83 GHz processing, the decrease in the temperature difference is rapid, and sign reversal (surface temperature being higher than the core temperature) is observed for 30 GHz processing at T = 950^{0}C and a heating rate of 75^{0}C/min. The magnitude of the temperature difference was observed to increase with the heating rate. Also measured were: (a) the densification curves for each of the microwave frequencies, (b) the dielectric permittivity of ZnO at a frequency of 2.45 GHz from room temperature and green-state density to 1200^{0}C where nearly theoretical density is achieved. These results suggest that simultaneous application of two or more widely separated frequencies is expected to allow electronic tailoring of the temperature profile during sintering.

A two dimensional code based on simultaneous solution of the heat equation and Maxwell's equations was developed. Taking into account were the dependence of the thermal, dielectric and densification properties of ZnO on temperature, density and frequency. A temperature feedback algorithm for controlling the microwave power, as in the experimental set-up, is also included. The computational results are in good agreement with the measurements, thus giving confidence in the code as a useful tool for understanding microwave sintering experiments. Simulations at various frequencies show that the temperature gradients developed with high frequency microwave sources are smaller than those obtained with low frequency (for the same T_{core} history),

and become negative at about 760 °C. The main change in behavior already occurs at 30 GHz and the difference between 30 and 83 GHz processing small (for ZnO). This is also observed experimentally as might be seen from Fig 5.

Acknowledgments

This work was supported by the Division of Advanced Energy Projects, U.S. Department of Energy, under grant number DE-FG02-94ER12190. Partial support provided by the Air Force Office of Scientific Research (MURI program on HPM), by the Air Force Office of Scientific Research (Directorate of Aerospace and Material Sciences), by the Army Research Office, by NATO Linkage Grant HTECH LG-940364 and by the Russian Basic Research Foundation, grant 95-02-05000-a. The authors are grateful to K. I. Rybakov and D. Abe for useful discussion and comments during this research.

Frequency [GHz]	Powder insulation	Control thermocouple	Process gas	Heating rate [^{0}C/min]
2.45	ZnO ($0.12\rho_{th}$)	core	air	1 ^{0}C/min to 200^{0}C then 15 ^{0}C/min
30	Al_2O_3 ($0.2\rho_{th}$)	surface	air	15,30&75 ^{0}C/min
83	Al_2O_3 ($0.2\rho_{th}$)	surface	air	15^0 C/min

Table I. Processing parameters for microwave sintering of ZnO at three frequencies

	Material	Density [g/cm^3]	Outer radius [cm]	Half height [cm]	N_r	N_z
Sample	ZnO	2.917	1.60	0.76	48	20
Powder Insulation	ZnO	0.673	2.54	7.00	78	50
Cast	Al_2O_3	0.240	3.81	8.25	92	60

Table II. Parameters used in the simulation. N_r and N_z are the accumulated cell numbers in the r and z directions.

References

1) Material Research Society Bulletin, Special Issue on Microwave Processing of Materials, **18**, 11 (1993)

2) D. Dadon, L.P. Martin, A. Birman, Y. Carmel, D. Gershon, J.P. Calame, B. Levush and M. Rosen "Temperature and Porosity Gradients Developed During Non-isothermal Microwave Processing of ZnO" J. Mat. Synth. and Proc. 4, 2, 1996.

3) A. Birman, B. Levush, Y. Carmel, D. Gershon, D. Dadon, L.P. Martin and M. Rosen, "Modeling of Multi-frequency Microwave Sintering of ZnO Ceramic" in Ceramic Transactions, **59**, Microwave: Theory and Application in Material Processing III., D. E. Clark, D. C. Folz, S. J. Oda and R. Silberglitt, eds. (American Ceramic Society, Cincinnati, OH, 1995), pp 305-312.

4) D. Dadon, Y. Carmel, A. Birman, D. Gershon, R. Hutcheon L.P. Martin, B. Levush and M. Rosen, "Electromagnetic Driven Heat Front during Microwave Heating of ZnO", submitted to Physical Review Letters.

5) L. P. Martin, D. Dadon, D, Gershon, M. Rosen, A. Birman, B. Levush and Y. Carmel: "Ultrasonic and Dielectric Characterization of Microwave and Conventionally Sintered ZnO", in press, J. Am. Ceramic. Soc. (October 1996)

6) M. Subirates,Y. Yao, M. Iskander and J. kiggans "FDTD Simulations of Microwave Sintering in Large (500/400 liter) Multimode Cavities", MRS Spring 1996 Meeting, san Francisco, April 8-12, paper O10.2, p 250.

7) L. Feher, G. Link and M. Thumm, "The Mira/Thesis-code for Resonator Design and Modeling of Millimeterwave Material Processing" MRS Spring 1996 Meeting, san Francisco, April 8-12, paper O16.5, p 255.

8) W. Sutton in Microwave Processing of Ceramic Materials, Am. Cer. Soc. Bull. 68, 376-85 (1989).

9) J. P. Calame, A. Birman, Y. Carmel, D. Gershon, B. Levush, A. A. Sorokin, V. Semenov, D. Dadon, L.P. Martin, M. Rosen: "A Dielectric Mixing Law for Porous Ceramics Based on Fractal Boundaries", J. Appl. Phys. 80, 7, 1996.

10) X. D. Yu, V. V. Varadan, V. K. Varadan, "Modeling Microwave Heating of Ceramic" in Ceramic Transactions, **21**, Microwave: Theory and Application in Material

Processing, D. E. Clark, F. D. Gac and W. H. Sutton, eds. (American Ceramic Society, Westerville, OH, 1991), pp. 167-176.

11) Y.S. Touloukian, R.W. Powell, C.Y. Ho, P.G. Klemens, "Thermophysical Properties of Matter" ,The TPRC Data Series (Plenum New-York 1970).

12) J.Wang and R. Raj, "Estimates of the Activation Energies for Boundary Diffusion from Rate-Controlled Sintering of Pure Alumina, and Alumina Doped with Zirconia or Titania." J. Am. Ceramic. Soc., **73**, pp. 1172-79, 1990.

13) R. Hutcheon, M. de Jong, F. Adams, G. Wood, J. McGregor and B. Smith, "A System for Rapid Measurements of RF and Microwave Properties up to 1400C", The Journal of Microwave Power and Electromagnetic Energy, **27** pp. 93-99 1992.

Figure caption

Figure 1. The skin depth normalized to the sample's radius (δ/r_{sample}) as a function of the temperature for ZnO at 2.45 GHz.

Figure 2. Diagram of the microwave sintering fixture. Sample diameter and height 3.2 and 1.524 cm. Inner diameter and height of the low density Alumina enclosure 5.08 and 14 cm. Outer diameter and height of the enclosure 7.62 and 16.5 cm.

Figure 3. Schematic diagram of the overmoded microwave processing furnace with a computerized feedback control of the temperature / microwave power.

Figure 4. Densification curves (Relative density, ρ/ρ_{th}) versus the maximum core temperature for ZnO samples sintered in microwave (2.45, 30, and 83 GHz) and thermal ovens.

Figure 5. The measured temperature difference ($\Delta T=T_{core} - T_{surface}$) versus T_{core} for ZnO. Data are for a heating rate of 15^0C/min at three different microwave frequencies (2.45, 30, and 83 GHz).

Figure 6. (a) The measured temperature difference ($\Delta T=T_{core} - T_{surface}$) for microwave sintering of ZnO at 30 GHz for two heating rates 15 ^{0}C/min and 75 ^{0}C/min. (b) same, but expanded scale.

Figure 7. The measured real (ε') and imaginary (ε'') parts of the complex permittivity of ZnO versus temperature at 2.45 GHz. The normalized skin-depth (δ/r_{sample}) is also shown.

Figure 8. Cell structure and notations used in the impedance matching solution for the electromagnetic wave within the sample and its insulation.

Figure 9. Measured parameters during the ZnO sintering process.

Figure 10. Comparison between the measured and the calculated parameters:

a. Calculated and measured T_{core} versus time.
b. Calculated and measured $T_{surface}$ versus time.
c. Calculated and measured temperature difference versus core temperature.
d. Calculated and measured microwave power versus time.

Figure 11. Calculated temperature difference ΔT versus core temperature for 2.45,30 and 83 GHz microwave frequency.

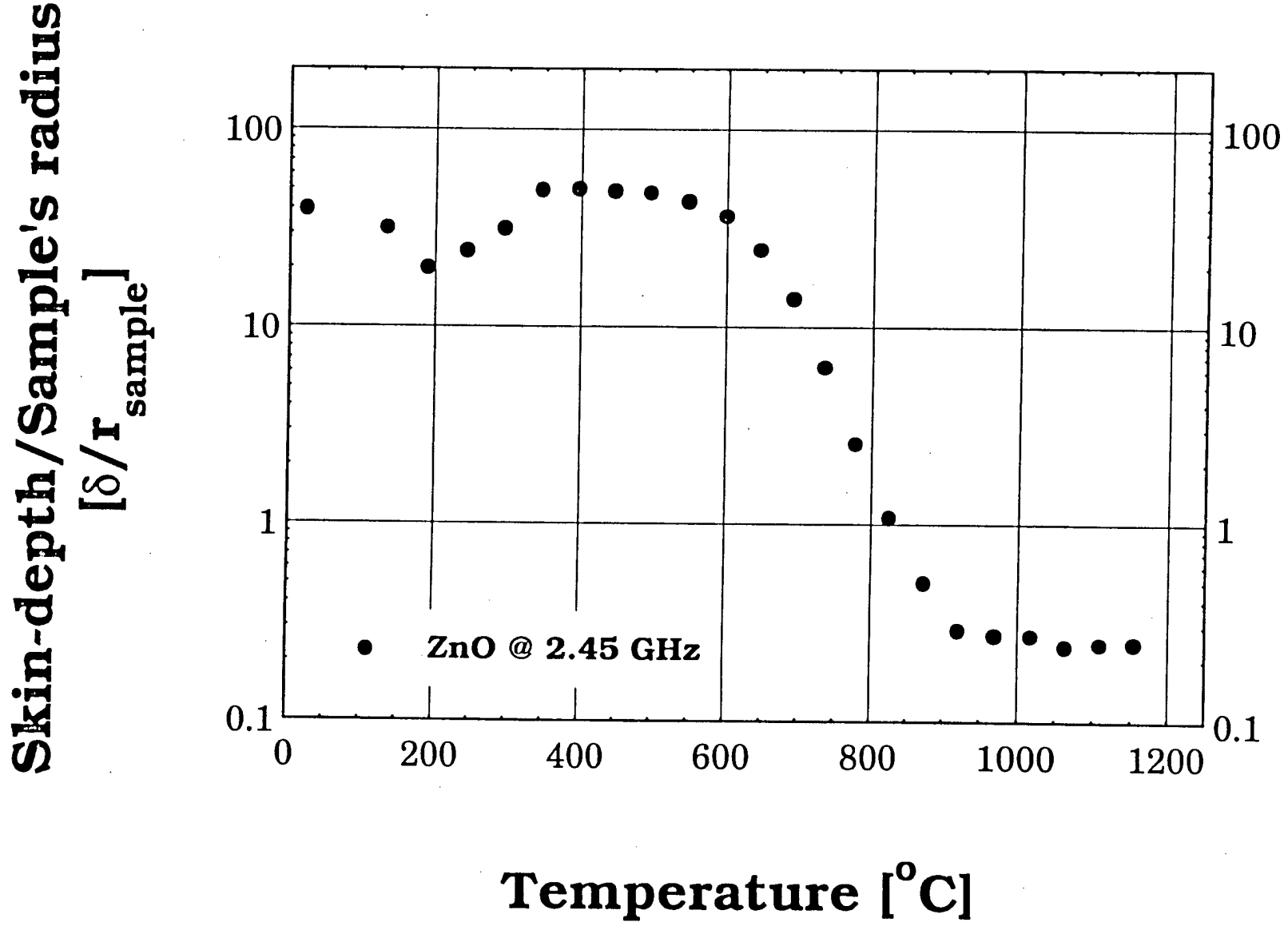
Skin-depth/Sample's radius
[δ/r sample]
100
10
1
0.1
0
200
400
600
800
1000
1200
ZnO @ 2.45 GHz
Temperature [°C]

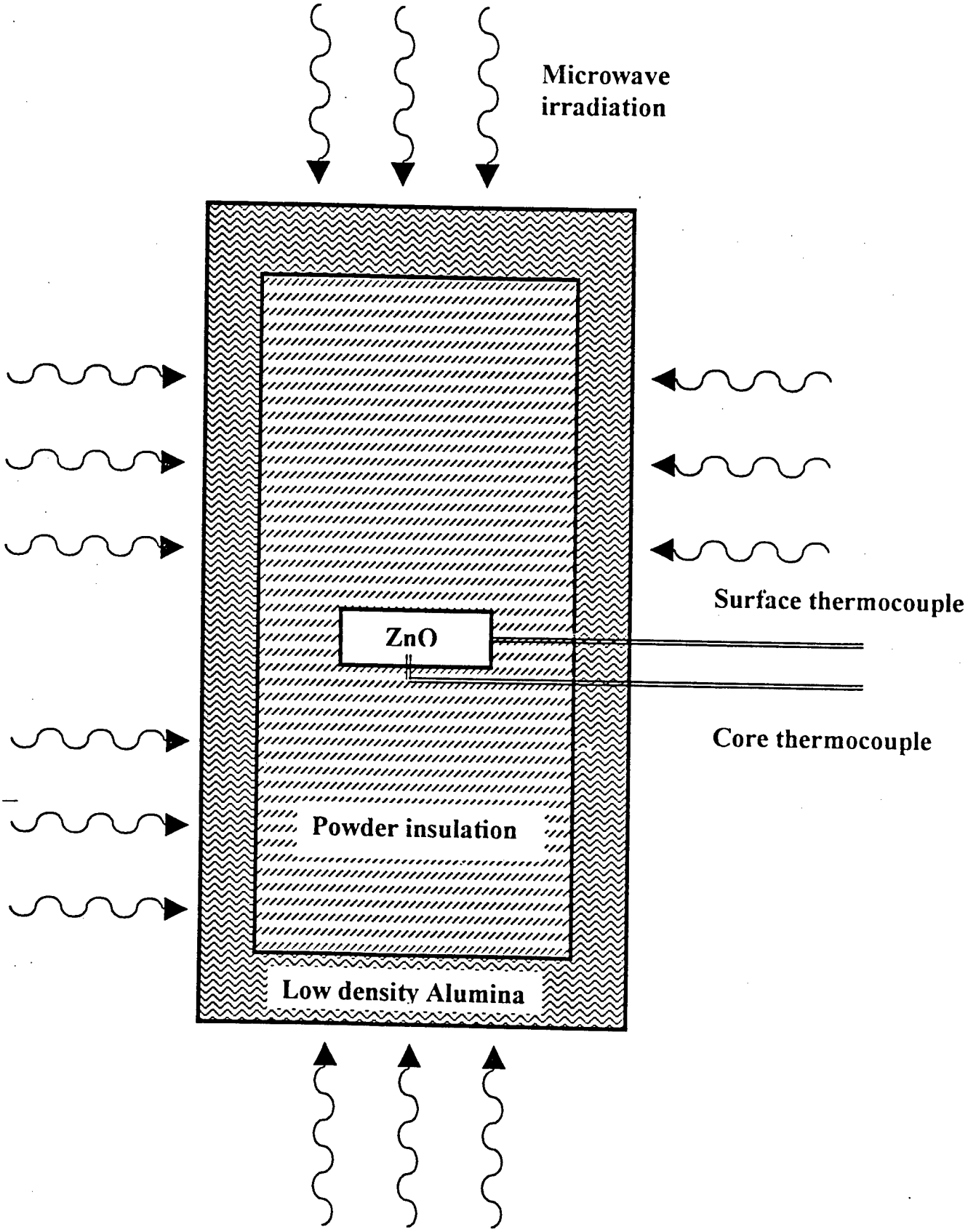
Microwave
irradiation
Surface thermocouple
ZnO
Core thermocouple
Powder insulation
Low density Alumina

Fig 2

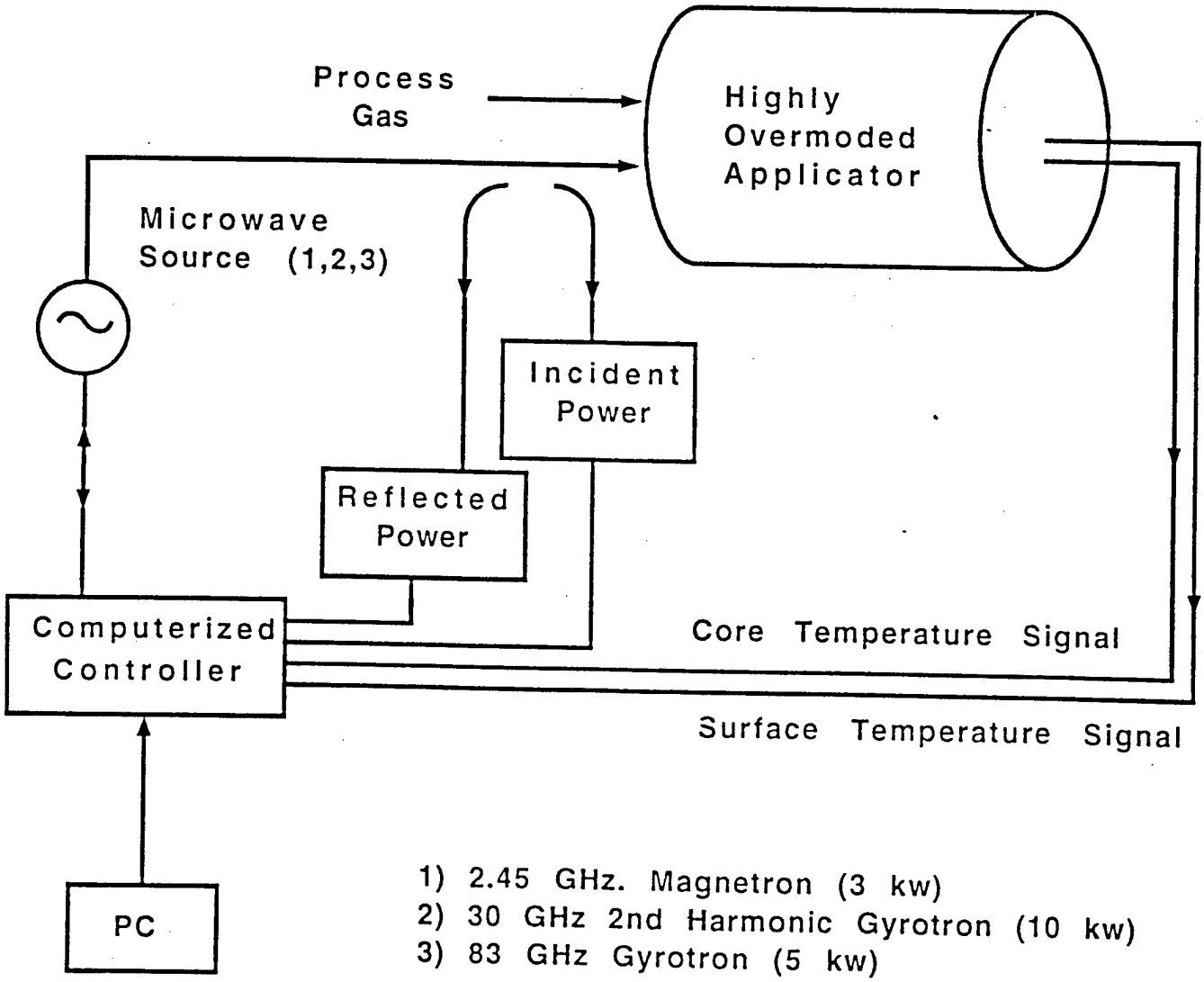

1) 2.45 GHz. Magnetron (3 kw)
2) 30 GHz 2nd Harmonic Gyrotron (10 kw)
3) 83 GHz Gyrotron (5 kw)

fig3

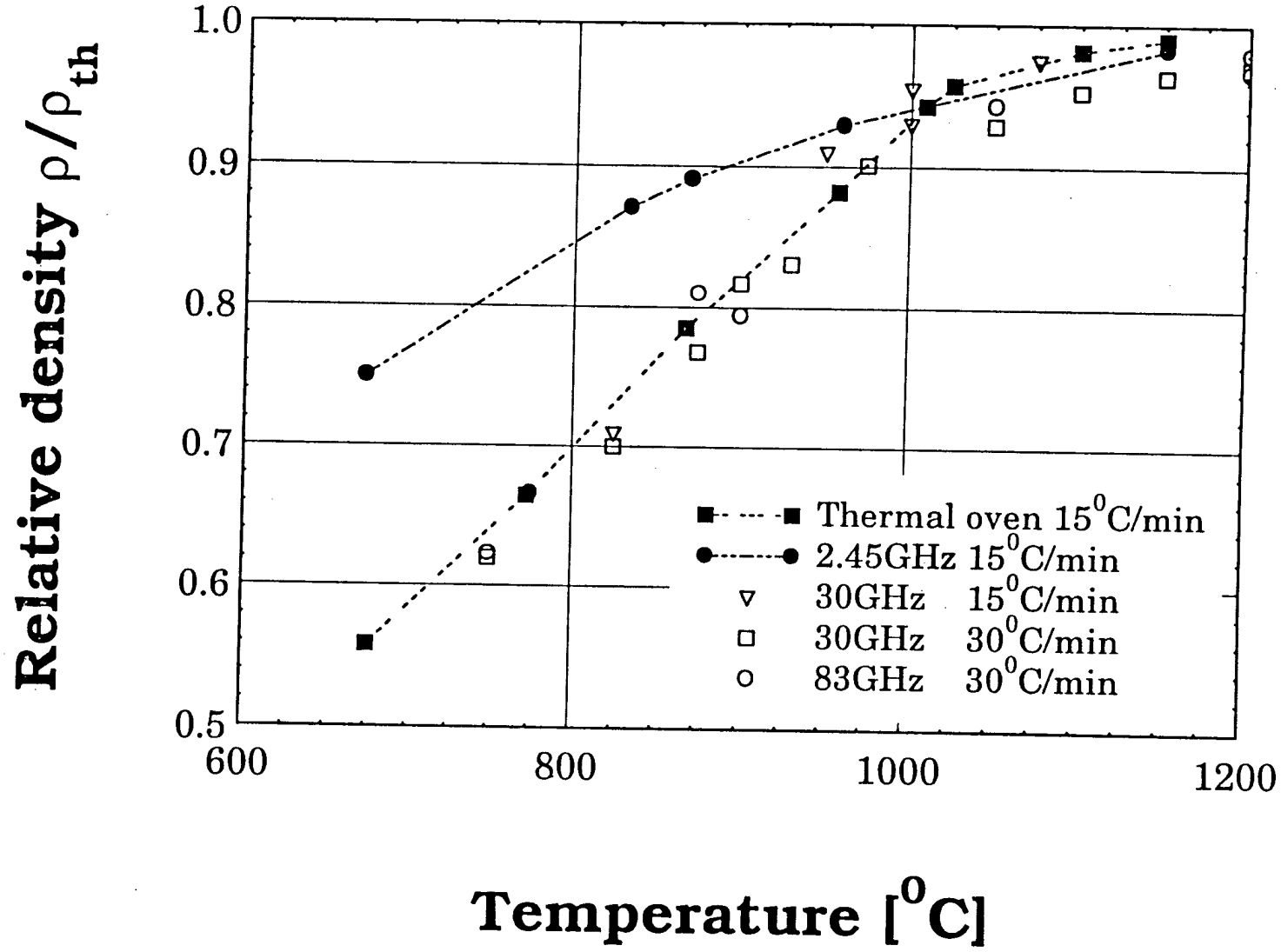
Relative density ρ/ρ_{th}
1.0
0.9
0.8
0.7
0.6
0.5
600
800
1000
1200
Thermal oven 15°C/min
2.45GHz 15°C/min
30GHz 15°C/min
30GHz 30°C/min
83GHz 30°C/min
Temperature [°C]

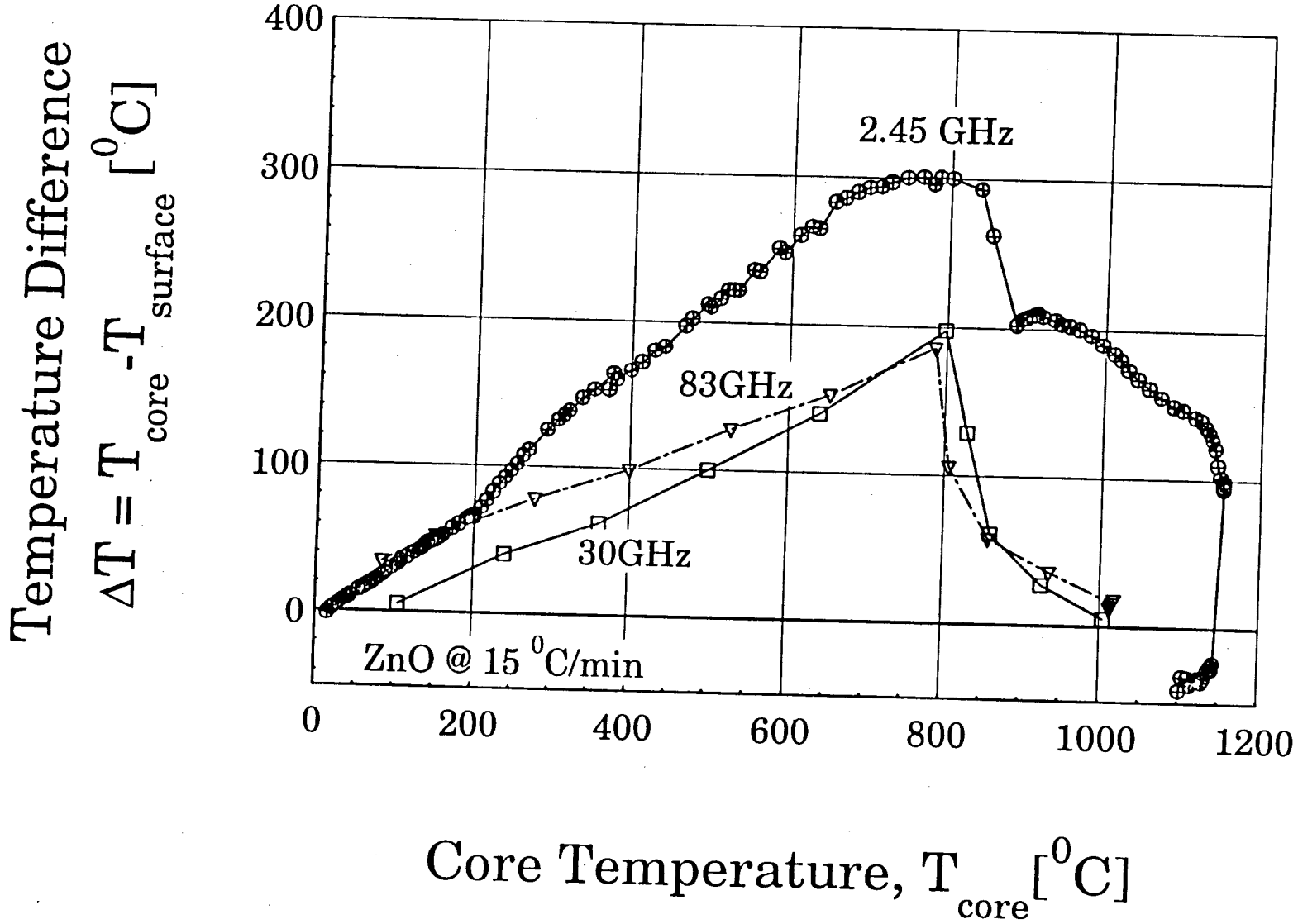
Temperature Difference
$\Delta T = T_{core} - T_{surface}$ [^{0}C]
400
300
200
100
0
2.45 GHz
83GHz
30GHz
ZnO @ 15 ^{0}C/min
0
200
400
600
800
1000
1200
Core Temperature, T_{core}[^{0}C]

Fig. 5

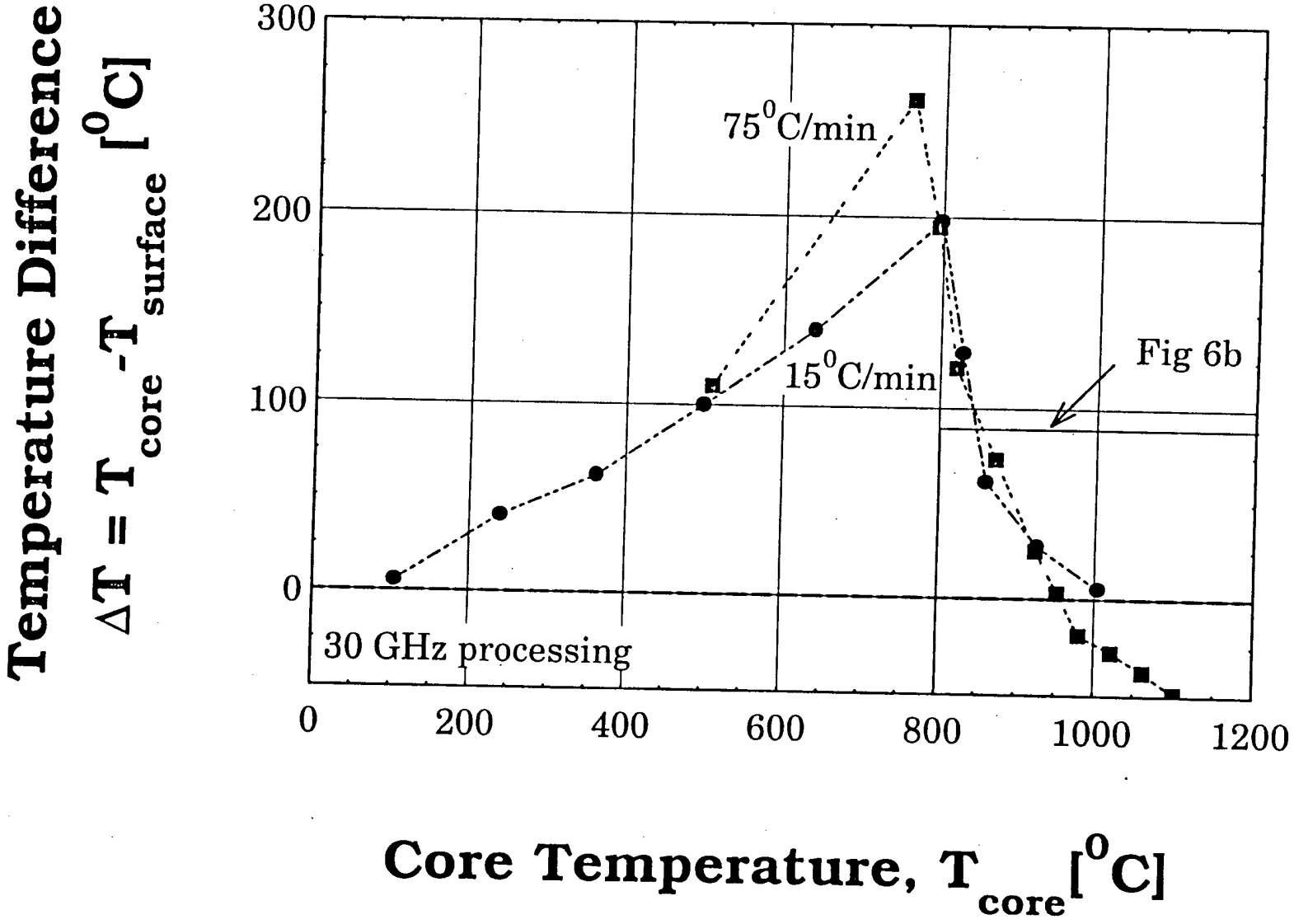
Temperature Difference
$\Delta T = T_{core} - T_{surface}$ [^{0}C]
300
200
100
0
75^{0}C/min
15^{0}C/min
Fig 6b
30 GHz processing
0
200
400
600
800
1000
1200
Core Temperature, T_{core}[^{0}C]

Fig. 6a

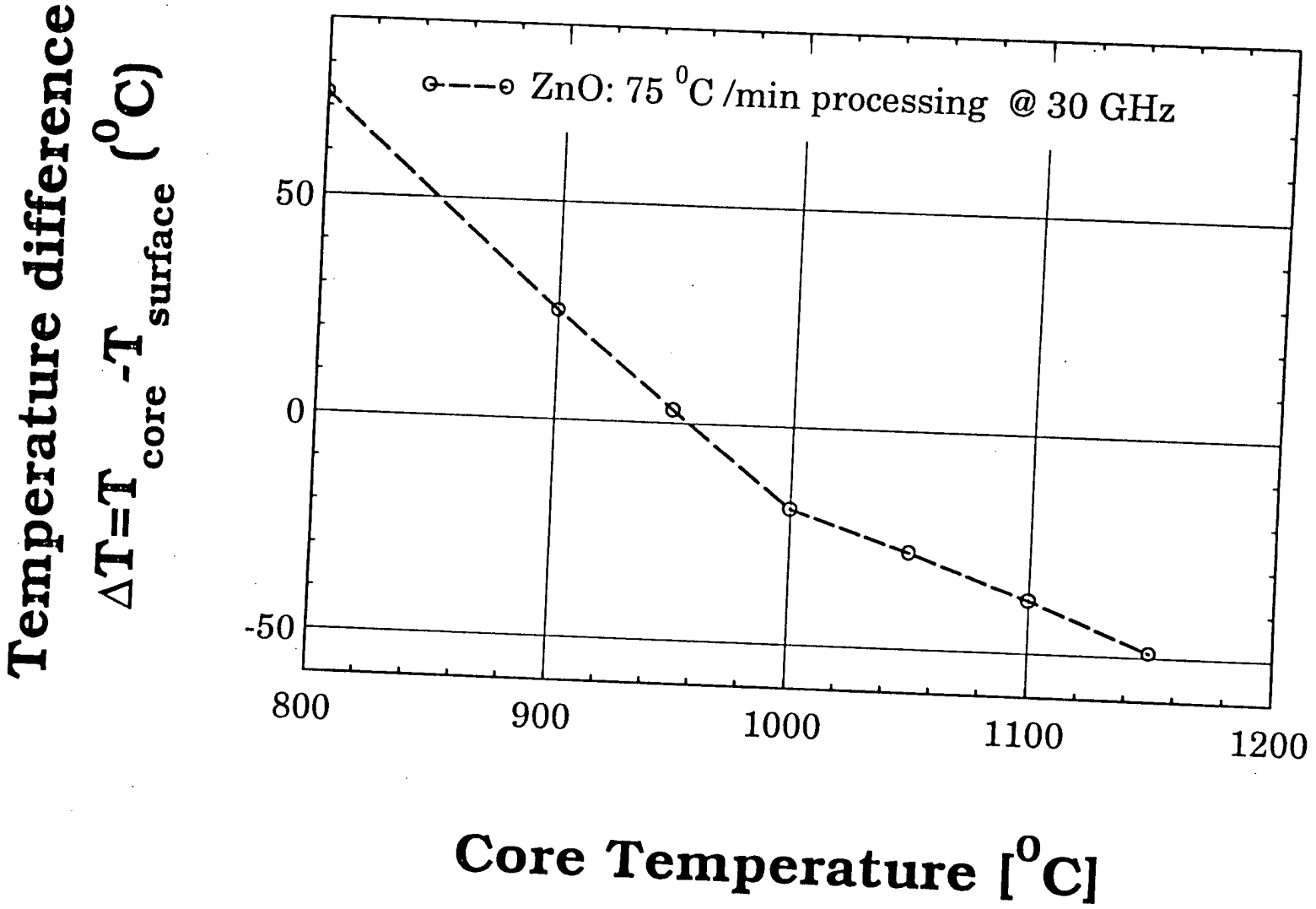
Temperature difference
$\Delta T = T_{core} - T_{surface}$ (^{0}C)
ZnO: 75 ^{0}C /min processing @ 30 GHz
50
0
-50
800
900
1000
1100
1200
Core Temperature [^{0}C]

Fig. 6b

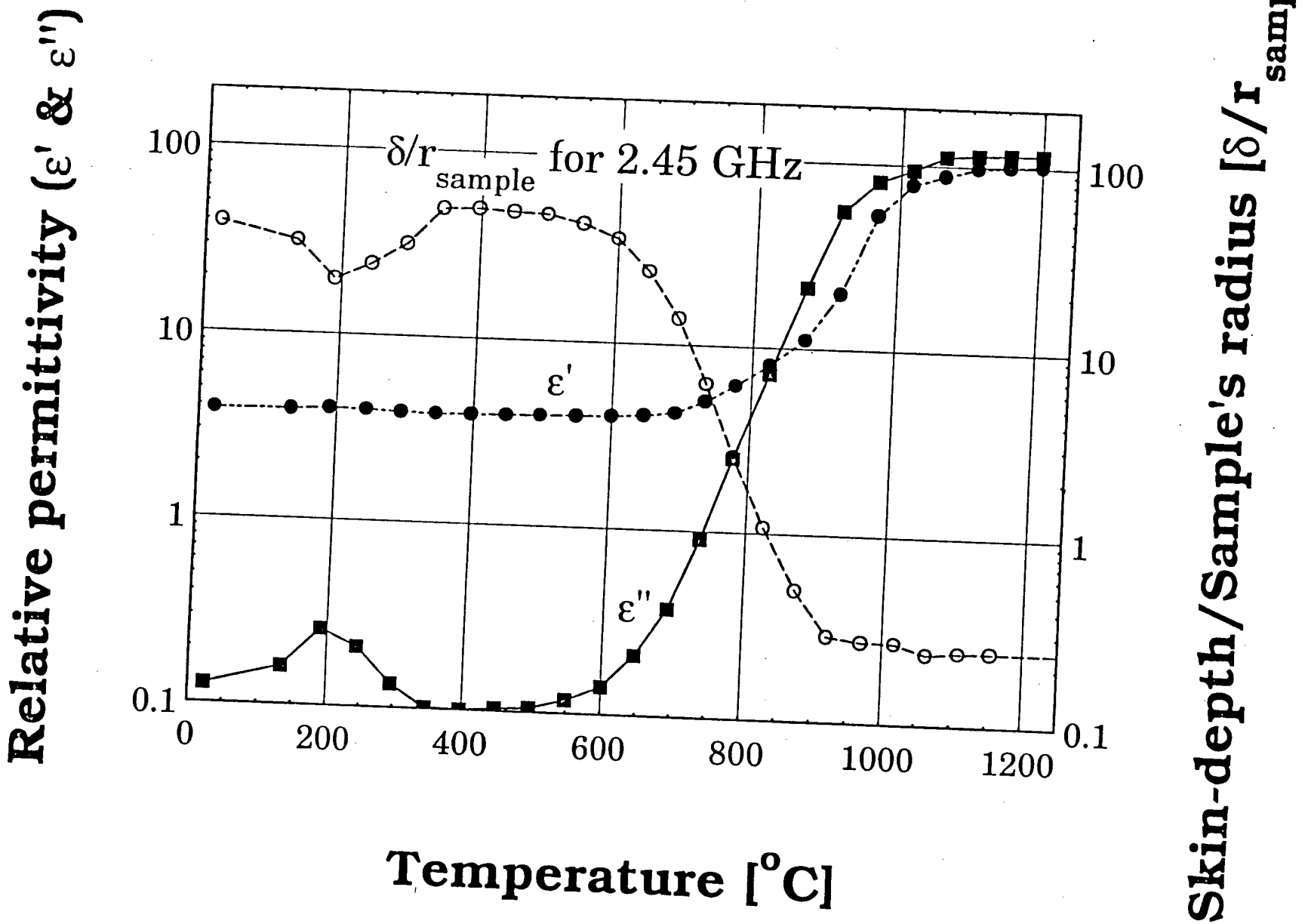
Relative permittivity (ε' & ε'')
Skin-depth/Sample's radius [δ/r sample]
δ/r sample for 2.45 GHz
ε'
ε''
100
10
1
0.1
0
200
400
600
800
1000
1200
Temperature [°C]

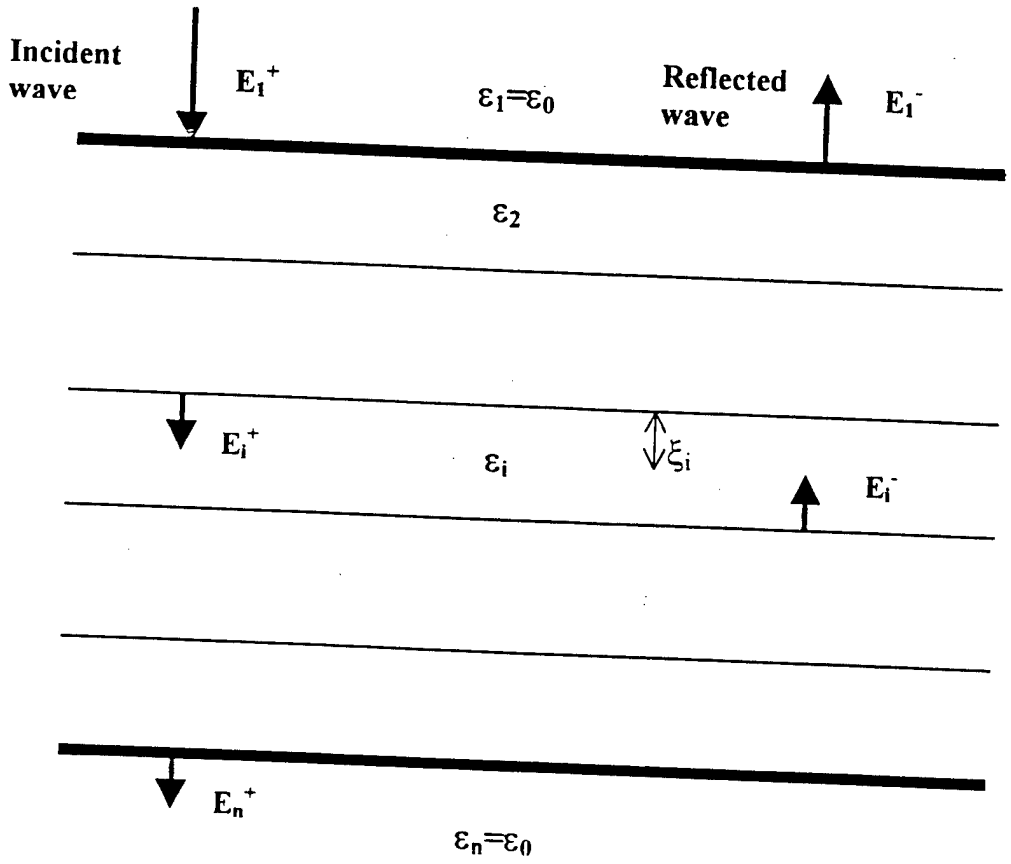
Incident wave
E_1^+
$\varepsilon_1=\varepsilon_0$
Reflected wave
E_1^-
ε_2
E_i^+
ε_i
ξ_i
E_i^-
E_n^+
$\varepsilon_n=\varepsilon_0$

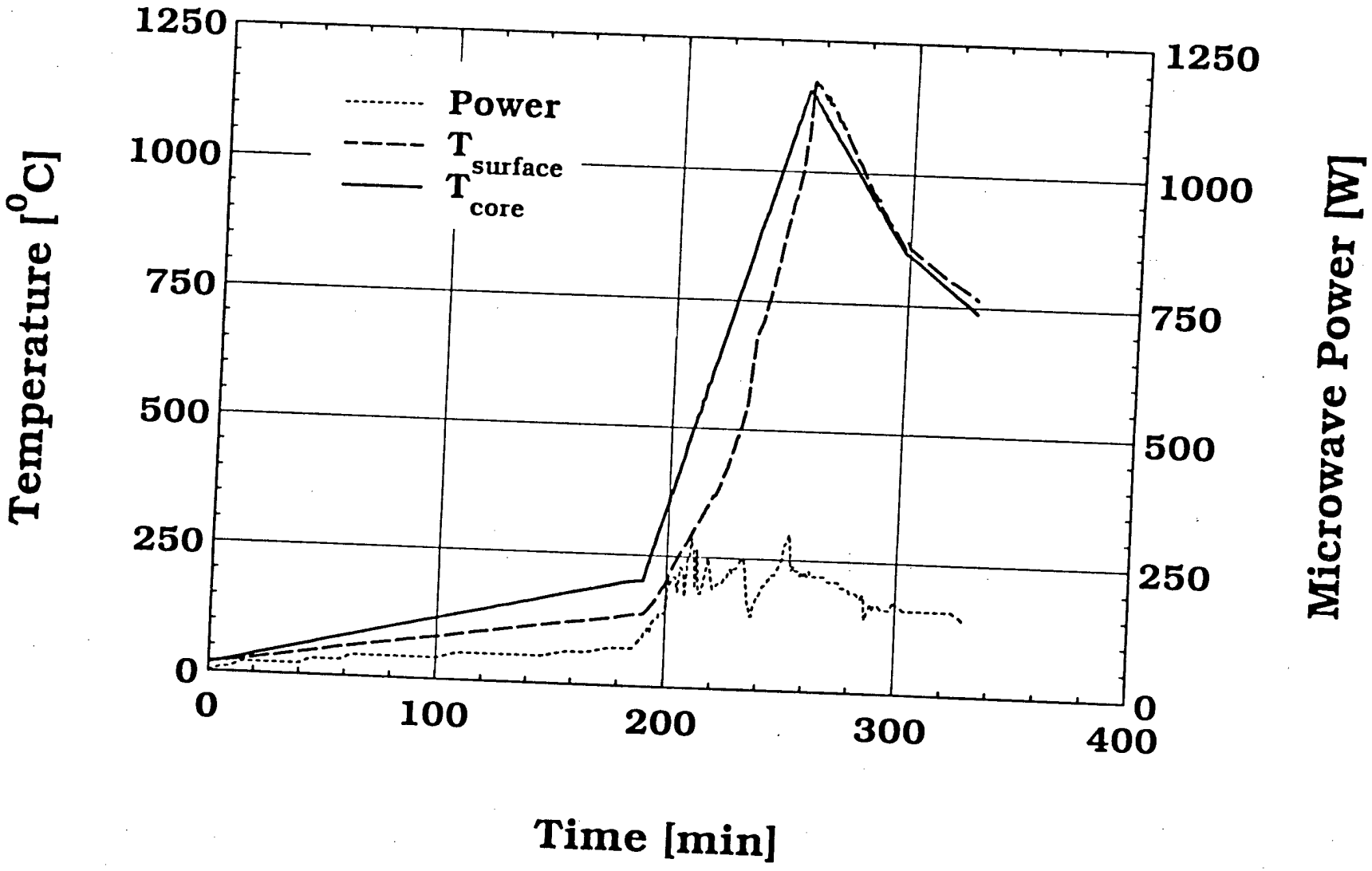
Temperature [^{0}C]
Microwave Power [W]
Time [min]
Power
$T_{surface}$
T_{core}
1250
1000
750
500
250
0
0
100
200
300
400

Fig. 2

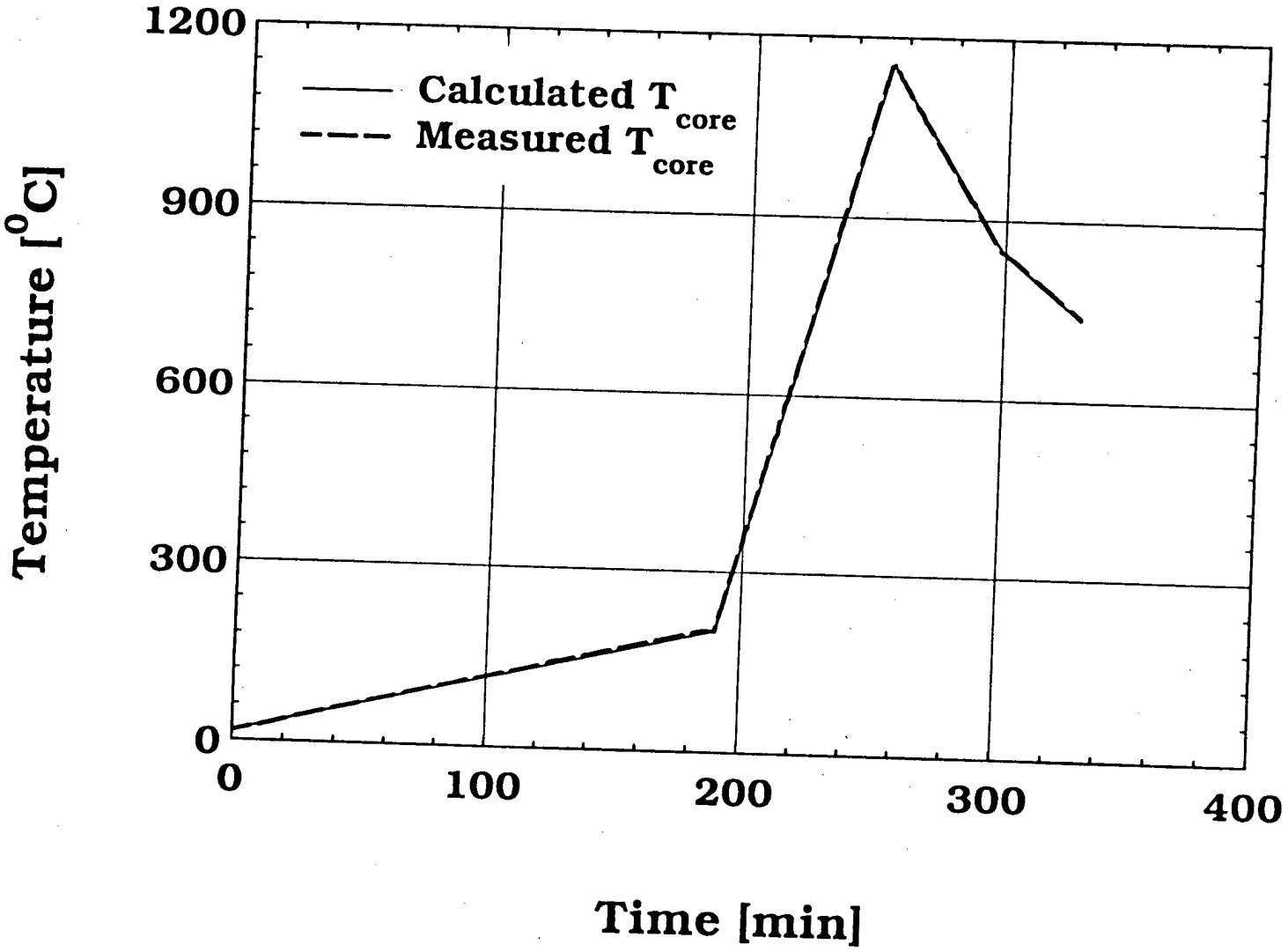
1200
900
600
300
0
0
100
200
300
400
Calculated T core
Measured T core
Temperature [0C]
Time [min]

Fig. 10a

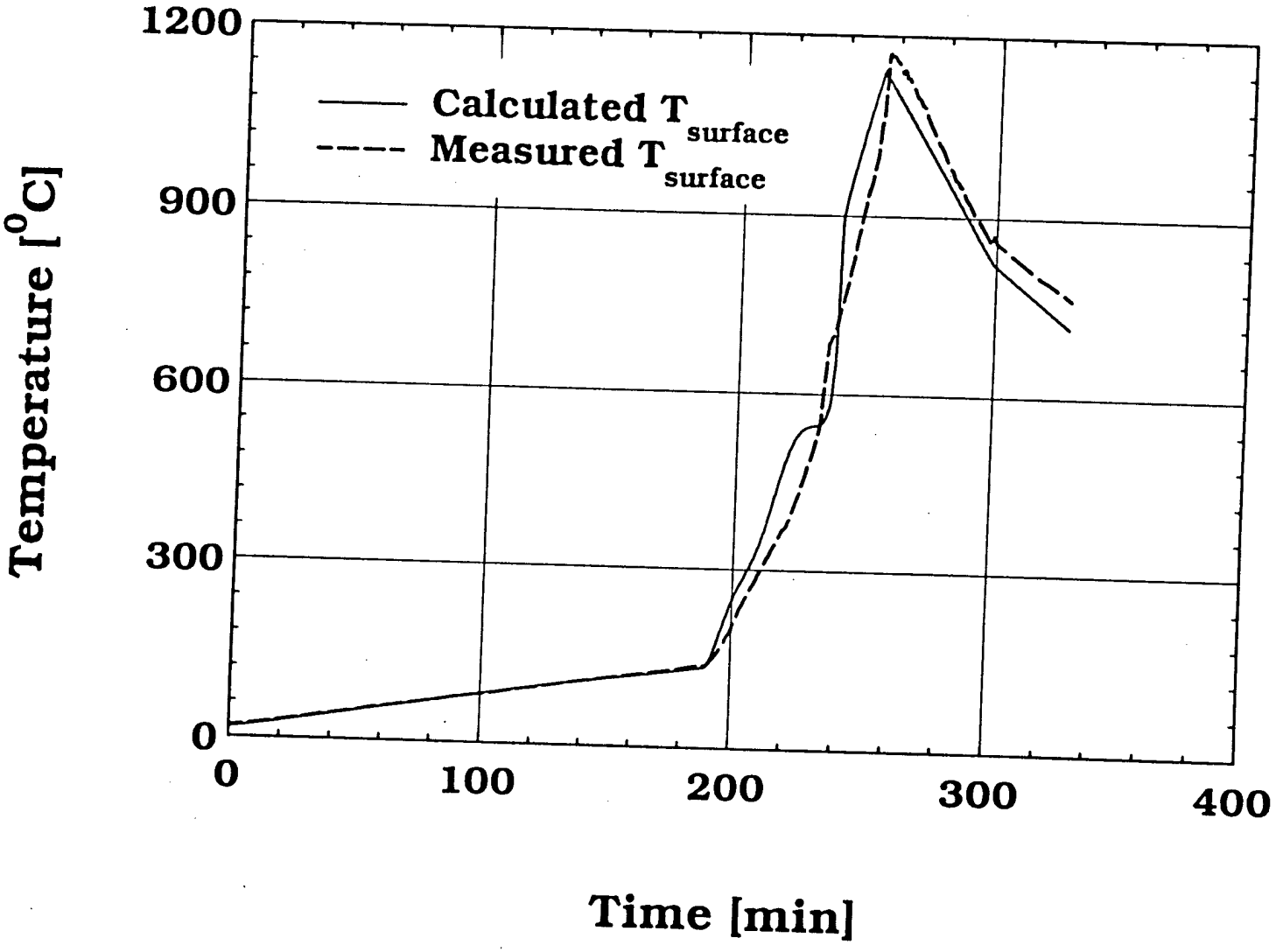
1200
900
600
300
0
0
100
200
300
400
Calculated T surface
Measured T surface
Temperature [0C]
Time [min]

Fig. 10 b

1997 Vac Elect Review

Low Cost Infrared Temperature Measurement and Optimal Process Control in Microwave Sintering Systems*

J.P. Calame, Y. Carmel, E. Pert, and D. Gershon
Institute for Plasma Research, Univ. of Maryland
College Park, MD 20742

Abstract

Ceramic sintering based on microwave heating has the potential to create final products with unique mechanical and electrical properties, including components for vacuum electronic RF devices. Such components include lossy ceramic composites for use as severs and mode control structures, ceramic insulators, and helix supports. The unique properties result from the rapid heating cycles which are made possible by the volumetric heating nature of microwaves. An important issue for industrial processing systems involves the non-contact measurement of temperature at multiple positions in a cost-effective manner. We have been experimentally investigating the application of direct detecting, commercial infrared thermocouples to this problem. We have designed and implemented a system using a series of these detectors in conjunction with movable gold mirrors and BaF_2 optical components (which operate to wavelengths as long as 20 microns). Experiments comparing the accuracy and reproducibility of this system to conventional thermocouples and optical pyrometers will be described for several materials.

Optimal control of the temperature depends on a detailed knowledge of the electromagnetic and thermal response throughout the object undergoing sintering. However, temperature can only be measured at a limited number of locations in the object; hence simulations must be used to infer what is happening in the rest of the object during the sintering process. Such complex simulations cannot be performed in real-time, but instead must be done prior to the sintering and used to form a processing plan of action for actual production. Real-time, closed loop process control can then be used to compensate for differences between reality and the simulations. This concept will be described.

* Work supported by AFOSR/MURI program on High Power Microwaves and an ARO STIR

Temperature Measurement

Temperature measurement in a sample undergoing microwave sintering can be measured by several techniques, including thermocouples, two color optical pyrometers, single color optical pyrometers, and infrared detectors. Although thermocouples are inexpensive ($10-$200) and very simple, they grossly distort the microwave fields near the sample, leading to vast gradients in power deposition, arcing, and extreme non uniform heating of the sample. Two color optical pyrometers are non-invasive and have very good accuracy, since type automatically compensate for differences in emissivity between materials, changes in emissivity as the sample densifies, and changes in optical system transmissivity over time. However, such systems are extremely expensive, ($4K-15K), and cannot operate below about 600 °C. The expense implies that having multiple temperature sensors for processing large and complex bodies will quickly become prohibitively expensive in an industrial system, and the lack of low temperature registration requires "blind" open loop control during critical stages of drying and volatile removal. Single

color optical pyrometers are more reasonable ($1K-2.5K), noninvasive, but also cannot operate below about 600 °C and are very sensitive to changes in emissivity and optical system transmissivity. As an alternative, we have been actively investigating a new device, known as an "Infrared Thermocouple", which consists of a non-invasive, direct IR detecting III-IV semiconductor diode. These devices are remarkably inexpensive ($400), and respond over a very wide 2-20 μm wavelength range. The ability to detect such long wavelength IR waves ensures a useful response down to 20 °C. Furthermore, the IR wavelengths are considerably larger than the typical 0.5-1.0 μm particle sizes used in ceramic green bodies. This has the advantage of creating insensitivity to changes in emissivity as the sample densifies. The low cost ensures that large numbers of these sensors can be economically used in a complex industrial furnace, while in a single sensor laboratory machine the temperature measurement system cost can be rendered insignificant.

To understand why such long wavelengths are required to register the low temperatures, one must consider the Plank blackbody radiation law

$$P_T(\lambda)d\lambda = \frac{8\pi hc}{\lambda^5}\frac{d\lambda}{e^{hc/\lambda kT}-1} \qquad (1)$$

The wavelength of peak radiation in microns is given by 2890/T, where T is the temperature in K. A series of these blackbody curves are shown in Fig 1. At 500 °C and below very little visible radiation is given off; the peak at 500 °C occurs at 3 μm, and at 20 °C the peak is at 10 μm. Also plotted in Fig 1 are the transmissivities for a 3 mm thick window of various IR materials.

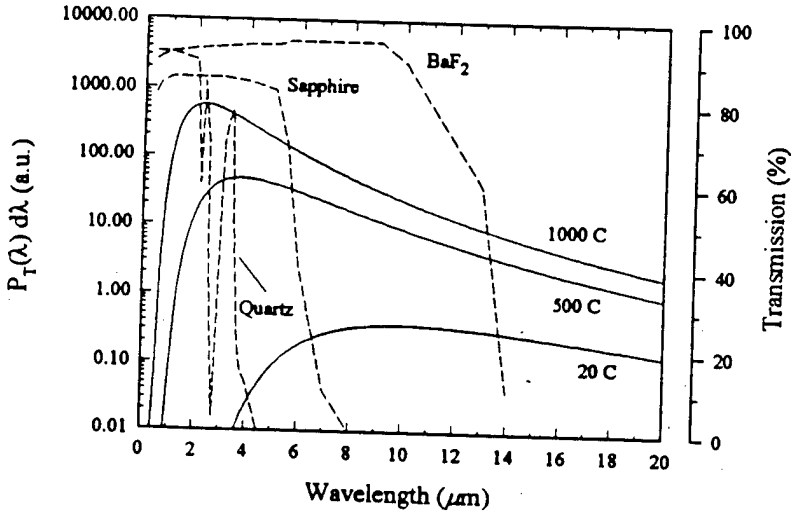

Figure 1. Blackbody curves at various temperatures and transmission of various materials

We have found that BaF_2 is the most suitable material for our system based on the requirement for long IR transmissivity, retention of visible range transmission, the ability to obtain commercial focusing lenses, and manageable sensitivity to humidity. A diagram of the temperature measurement setup within the microwave furnace is shown in Fig. 2. These "infrared thermocouples" combined with the optical system must be calibrated against an ordinary thermocouple for each specific material to be processed. We have performed such calibrations for

ZnO and Al_2O_3, and we have found insignificant variation from sample to sample (of a given material composition) once this procedure was carried out. This ensures that in a final system a "library" of calibration data for various materials can be created and used by the operator in planning a thermal processing cycle. An example of such a calibration run is shown in Fig. 3.

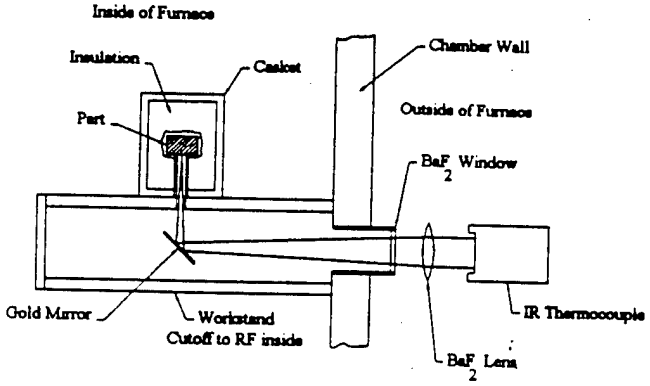

Figure 2. Diagram of the temperature measurement optical system

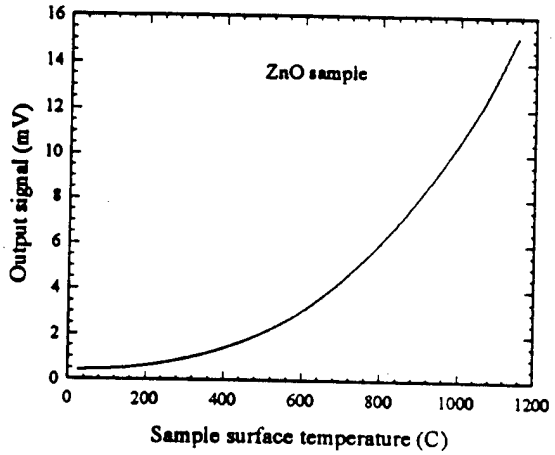

Figure 3. Typical calibration curve obtained with the optical system

Optimal Control of Microwave Sintering Systems

A diagram of a simple proportional-integral-differential control system for a microwave sintering system is pictured in Fig 4. The complex thermal behavior of the sample consists of many details, such as how the microwaves are distributed inside the sample, the dielectric properties, and the thermal properties. All of these change with time as the sample densifies. Thus we have a nonlinear, time-dependent system. If the exact behavior of the system could be modeled accurately, then open loop control could be used. However, the complexity of the system requires the use of feedback to allow tracking of desired temperature profiles vs. time. Even so, obtaining good feedback control through selection of a control scheme and proper adjustment of the controller settings is a non-trivial issue in a complex nonlinear system. This is particularly true if the ceramic undergoing processing has material and dimensional properties which change over broad ranges as the processing proceeds. Many large and complex ceramic bodies are very expensive to make, which rules out extensive trial and error adjustment methods. To address these problems, we have been exploring the use of computer simulations of the sintering behavior of ceramics, in order to select control architecture and coefficients prior to actually processing a real body. Properly done, such a procedure ensures much tighter closed-loop control than normally achievable.

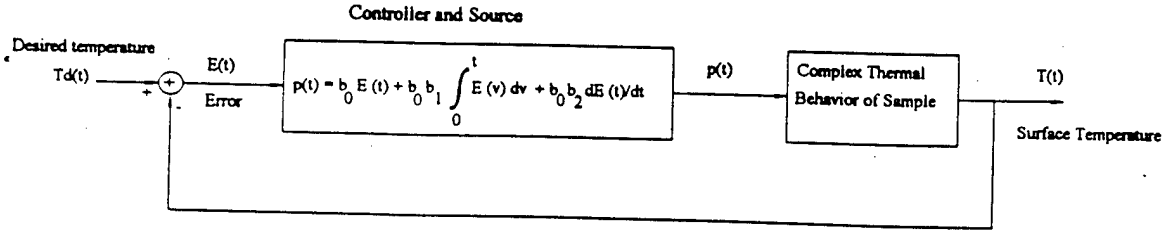

Figure 4. Block diagram of a simple control scheme for a microwave sintering system

To accomplish such modeling, the ceramic body is divided up into meshes suitable for finite difference or finite element modeling. At any given time the meshes are assigned an appropriate set of dielectric and thermal properties depending on the temperature and density of the mesh element. The electromagnetic fields throughout the body are solved by finite element analysis, leading to a known power deposition in each mesh. These power densities are used in conjunction with the current temperatures to get new temperatures, by solving the time dependent heat equation. Similarly, the densification and therefore shrinkage is modeled with a densification equation. The process is then repeated. Obviously such a computation is very difficult in full 3D, so we have been concentrating on 1D slab models at present. Figure 5 shows the results of simulations of a 3.3 cm thick slab of initially 52% dense ZnO pressed ceramic body surrounded by 4 cm of 12% density ZnO powdered insulation, when subjected to a surface power density $P_s(t)$ (W/m^2) that linearly increases with time according to $P_s(t)=Rt$. Simulated results of core and surface temperatures for R = 300 and 600 $Wm^{-2}s^{-1}$ are shown.

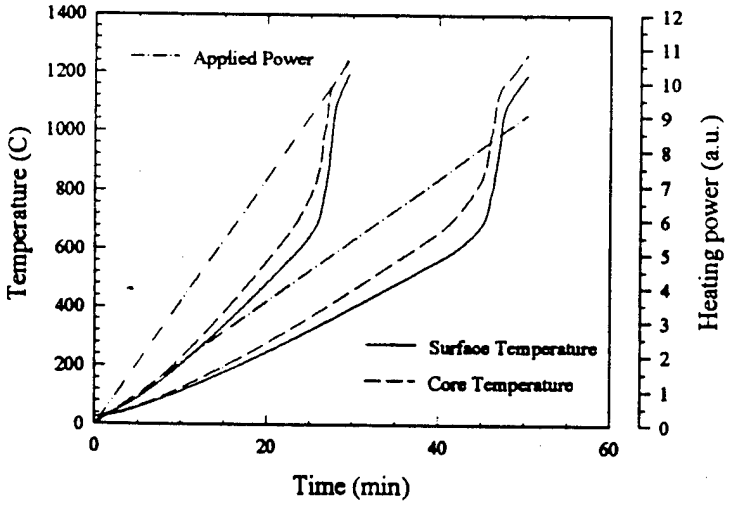

Figure 5. Results of simulations of zinc oxide sintering with linearly increasing applied power

To investigate how to set up the control system, these simulations were used in conjunction with a simple first order nonlinear model of the ceramic system behavior

$$\frac{dT(t)}{dt} = a_0(T)p(t) - a_1(T)T(t) \quad . \qquad (2)$$

At any given temperature and time the linearized Laplace transform model for the ceramic was approximated by

$$F(s) = \frac{a_0}{s + a_1} \quad . \qquad (3)$$

From an analytical control system analysis the transfer behavior of a PI (proportional-integral), incrementally linear control system under these assumptions was found to be given by

$$\tilde{T}(s) = \frac{a_0 b_0 (s + b_1)}{s^2 + (a_1 + a_0 b_0)s + b_1 a_0 b_0} \tilde{T}_d(s) \quad , \qquad (4)$$

where the PI control function was assumed to be $C(s) = b_0 + b_0 b_1/s$, and derivative control was not employed at this point. The gain (proportional) coefficient b_0 was using proportional band formalism (B_p) equal to 5% of the span, and the integral term was selected to create optimal damping of transients. The relevant equations are

$$b_0 = \frac{\left(\left. \frac{dT}{dt} \right|_{\max} + a_1 T_m \right)}{a_0 T_m B_p} \qquad b_1 = \frac{(a_1 + a_0 b_0)^2}{2 a_0 b_0} \qquad (5,6)$$

where T_m is the maximum desired temperature and dT/dt is the maximum desired heating rate. For nonlinear optimal control, these coefficients b_i would be functions of temperature since a_i are temperature dependent. We have found that for the simple example presented here that it suffices to simply set the a_i in the above equations to constants equal to the average values of the $a_i(T)$ over the relevant range of temperatures, to arrive at constant control coefficients. Simulated results of this procedure are shown in Fig 6, for a constant rate heating profile $T_d(t)$ of 60 °C/min. Clearly the surface temperature follows an appropriate linear ramp. In future work on complex bodies exhibiting more drastic temperature variations we will undoubtedly need to utilize the more general nonlinear, optimal control scheme in which the b_i are allowed to vary (in the manner that the simulations predict) as the process proceeds.

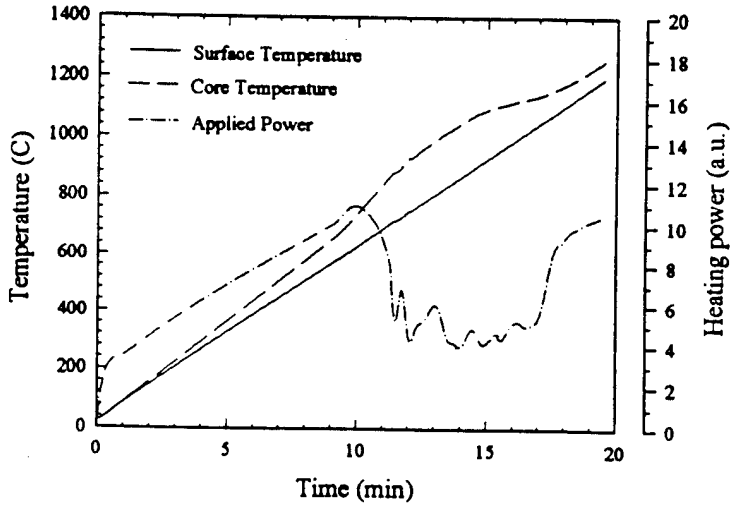

Figure 6. Simulation with optimal PI control at 60 C/min.

Due to the self insulating properties of ceramic materials, coupled with the volumetric nature of the microwave heating process, core temperatures exceed surface temperatures. This is clearly seen in the Fig. 6 simulations. Such gradients are also observed in experiments. One way to prevent gradients is to apply a conventional heat source to the surfaces of the ceramic undergoing

sintering, in addition to the volumetrically applied microwaves. If both the surface and core temperatures were known, then a more complex control system could actuate both the conventional and microwave heating to cancel the thermal gradients and control the temperature vs. time profile. Unfortunately, it is not possible to measure the internal temperatures of the part directly. However, as has been shown here it is possible to approximately simulate the behavior of inaccessible regions of the system on a computer. An interesting problem is to create a simple model that estimates the core temperature based on the measured surface temperature, the microwave power being injected at the sample, and various histories of these quantities. Such a model can be designed using the simulations and applied in real time to an actual component. One example of such an estimator for the core temperature $T_c(t)$ is

$$T_c(t) = e_0(T)T(t) + e_1(T)p(t) + e_2(T)\int_0^t p(v)\frac{dT(v)}{dt}dv \qquad (7)$$

where $T(t)$ is the measured surface temperature and $p(t)$ is the power injected into the processing chamber. The temperature dependent values of $e_i(T)$ can be determined from simulations. An example of the simulated results using such an estimator are shown in Fig. 7. In one curve the simulation for the core temperature is shown, and the other curve is the prediction of the estimator. Clearly this procedure is promising. Current investigations are focusing on developing estimators that are insensitive to errors between the computer model of the sintering process and reality (such as the exact variation in dielectric loss with temperature). We are currently applying microwave sintering and the techniques discussed in this paper to develop a zero porosity, Al_2O_3-carbon composite microwave absorber for HPM devices. Future work will concentrate on the development of environmentally safe AlN-SiC absorbers for high rep-rate 94 GHz radar sources.

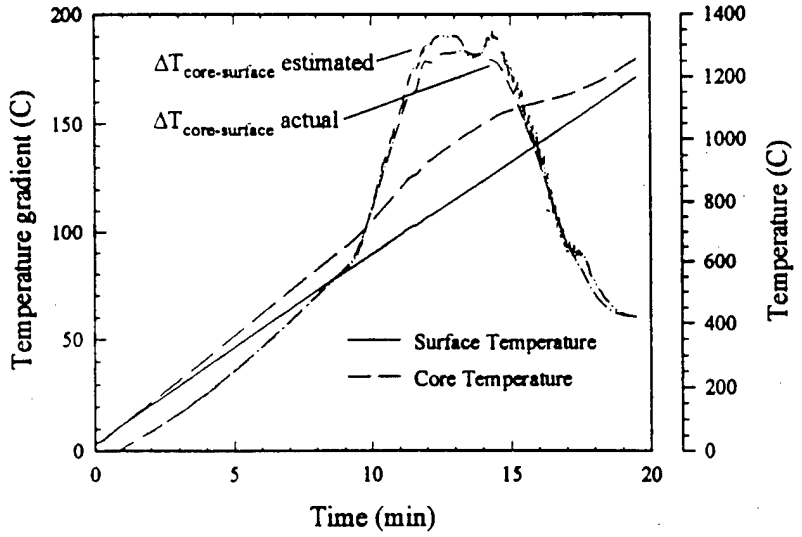

Figure 7. Simulations comparing modeled core temperature with core temperature from the estimator